

A New Single-Layer Urban Canopy Model for Use in Mesoscale Atmospheric Models

YOUNG-HEE RYU, JONG-JIN BAIK, AND SANG-HYUN LEE*

School of Earth and Environmental Sciences, Seoul National University, Seoul, South Korea

(Manuscript received 29 September 2010, in final form 25 May 2011)

ABSTRACT

A new single-layer urban canopy model for use in mesoscale atmospheric models is developed and validated. The urban canopy model represents a built-up area as a street canyon, two facing buildings, and a road. In this model, the two facing walls are divided into sunlit and shaded walls on the basis of solar azimuth angle and canyon orientation, and individual surface temperature and energy budget are calculated for each wall. In addition, for better estimation of turbulent energy exchange within the canyon, a computational fluid dynamics model is employed to incorporate the effects of canyon aspect ratio (height-to-width ratio) and reference wind direction on canyon wind speed. The model contains the essential physical processes occurring in an urban canopy: absorption and reflection of shortwave and longwave radiation, exchanges of turbulent energy and water between surfaces (roof, two facing walls, and road) and adjacent air, and heat transfer by conduction through substrates. The developed urban canopy model is validated using datasets obtained at two urban sites: Marseille, France, and Basel, Switzerland. The model satisfactorily reproduces canyon air temperatures, surface temperatures, net radiation, sensible heat fluxes, latent heat fluxes, and storage heat fluxes for both sites. Extensive experiments are conducted to examine the sensitivities of the urban surface energy balance to meteorological factors and urban surface parameters. The reference wind speed is found to be a more crucial meteorological factor than the reference air temperature in altering urban surface energy balance, especially for weak winds. The urban surface energy balance is most sensitive to the roof albedo among urban surface parameters. The roof fraction, canyon aspect ratio, and ratio of roughness length for momentum to that for heat for the roof play important roles in altering urban surface energy balance.

1. Introduction

Urban impacts on weather and climate have recently received considerable attention. Many observational and numerical modeling studies have been performed to document atmospheric phenomena peculiar to urban areas and to understand the physical processes that are involved. These phenomena include urban heat islands, urban breezes, urban-induced or urban-modified clouds and precipitation, and turbulent flows over cities. Comprehensive reviews on these subjects are given in Roth (2000), Arnfield (2003), Shepherd (2005), Masson (2006), and Kanda (2007).

Mesoscale atmospheric models are a useful tool for studying urban impacts on weather and climate. For the reliable simulation or prediction of weather and climate in urban areas, mesoscale atmospheric models are required to be urbanized well; that is, physical processes occurring at and near urban surfaces should be included properly in models. Current mesoscale atmospheric models cannot explicitly resolve urban canopies (e.g., urban canyons and buildings) in the horizontal direction, and therefore parameterized physical processes are inherently subgrid-scale processes.

A traditional and simple method for representing urban effects in mesoscale atmospheric models is to use slab models. Slab models do not consider an urban canopy but simply change surface properties such as albedo, roughness length, surface moisture availability, thermal conductivity, and heat capacity. Slab models are known to fail in simulating some characteristic features of, for example, nighttime energy balance (Kusaka et al. 2001) and mean wind and turbulence (Coccal and Belcher 2004).

To overcome drawbacks in slab models, urban canopy models (UCMs) have been developed in the past

* Current affiliation: NOAA/Earth System Research Laboratory, and Cooperative Institute for Research in Environmental Sciences, University of Colorado, Boulder, Colorado.

Corresponding author address: Jong-Jin Baik, School of Earth and Environmental Sciences, Seoul National University, Seoul 151-742, South Korea.
E-mail: jjbaik@snu.ac.kr

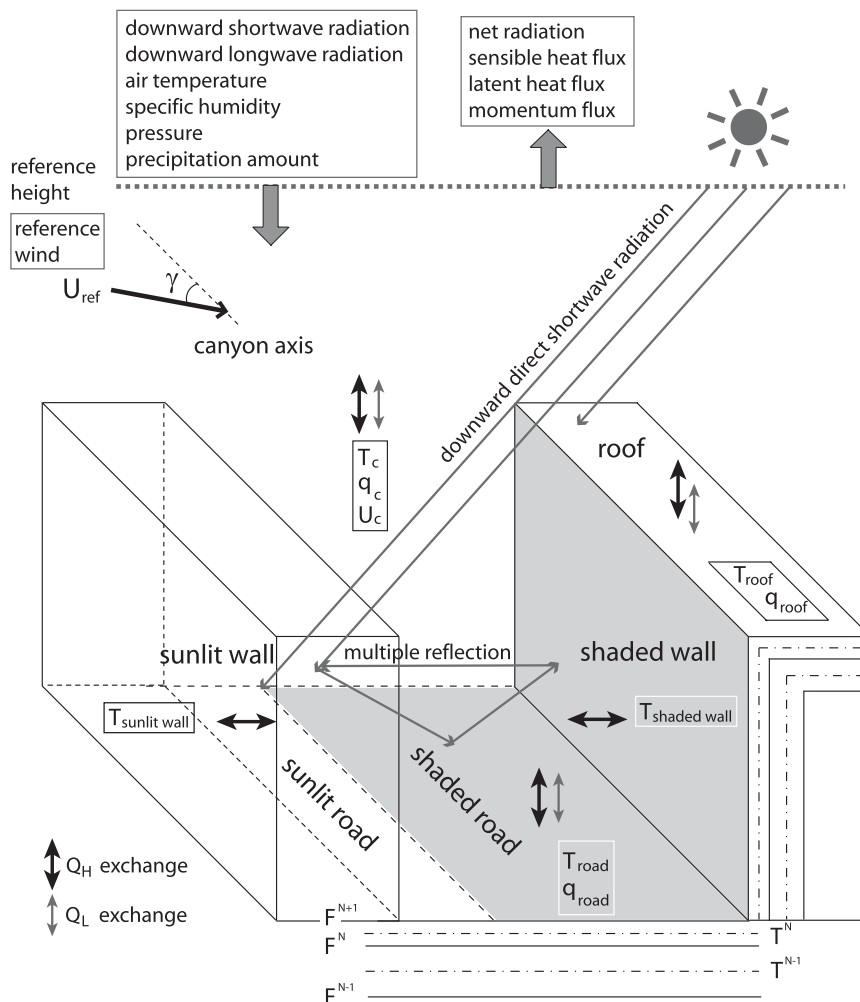


FIG. 1. An illustration of the single-layer urban canopy model. See text for details.

decade. Current UCMs can be categorized into the single-layer UCM (Masson 2000; Kusaka et al. 2001; Dupont and Mestayer 2006; Lee and Park 2008; Oleson et al. 2008) and multilayer UCM (Ca et al. 1999; Martilli et al. 2002; Dupont et al. 2004; Otte et al. 2004; Kondo et al. 2005). Both the single-layer and multilayer UCMs consider an urban canyon and active surfaces (road, wall, and roof). A main difference between the single-layer and multilayer UCMs lies in the representation of the vertical structure of the urban canopy (Masson 2006). Single-layer UCMs treat an urban canyon as a single layer and a wall surface as a single representative wall surface. In contrast, in multilayer UCMs an urban canyon is divided into multiple layers and a wall surface is divided into multiple wall surfaces in the vertical direction.

We have developed a new single-layer UCM that can be used in mesoscale atmospheric models. The UCM

developed in this study is designed to provide bottom boundary conditions of radiative, heat, moisture, and momentum fluxes for a mesoscale atmospheric model. In this model, a number of important physical processes occurring in an urban canopy are parameterized. Figure 1 illustrates the various physical processes, input variables from a mesoscale atmospheric model, output variables from the UCM, and internal variables explicitly calculated in the UCM. The UCM is developed based on the vegetated single-layer urban canopy model of Lee and Park (2008), but the vegetation part is excluded. We treat a built-up area and a natural area (e.g., vegetation) separately and combine their effects in a tile approach.

One of the salient features of our proposed UCM is that two facing walls are separated into sunlit and shaded walls. For example, in the morning, the east-facing wall for a north–south-oriented canyon is set as

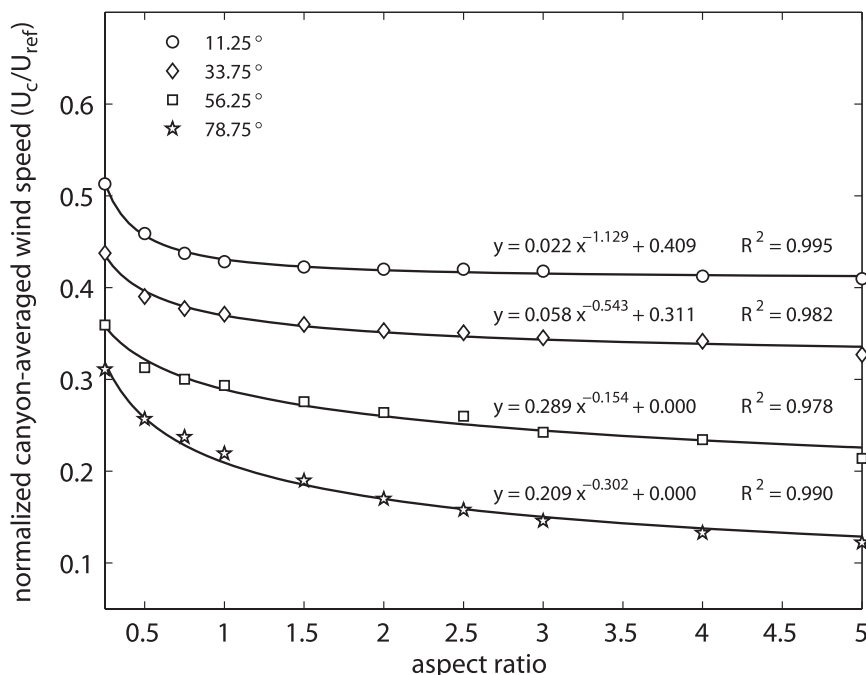


FIG. 2. Normalized canyon wind speeds according to canyon aspect ratios for various relative reference wind directions. Markers and lines indicate CFD-model simulation results and corresponding fitting functions, respectively. Here, R^2 is the coefficient of determination.

a sunlit wall and the opposite west-facing wall is set as a shaded wall. In other words, sunlit and shaded walls correspond to specific walls. This feature is different from that of Oleson et al.'s (2008) approach. Oleson et al. distinguish sunlit and shaded walls but do not match them with specific walls. In previous single-layer UCMs (Masson 2000; Kusaka et al. 2001; Lee and Park 2008) except for Oleson et al.'s (2008) model, two facing walls are not separated into sunlit and shaded walls but are regarded as the same wall.

Another salient feature is that the effects of canyon aspect ratio (height-to-width ratio) and reference wind direction relative to canyon orientation on canyon wind speed are included. The canyon wind speed is a crucial factor in calculating surface energy fluxes within an urban canyon. The effect of canyon aspect ratio on street-canyon flows has been demonstrated indirectly through the time constant (Lee and Park 1994), residue pollutant concentration (Kim and Baik 1999), and transfer coefficient (Barlow and Belcher 2002). A few studies have quantitatively investigated the effect of canyon aspect ratio on canyon wind speed (Swaid 1993; Lemonsu et al. 2004). In previous single-layer UCMs (Masson 2000; Kusaka et al. 2001; Lee and Park 2008; Oleson et al. 2008), the effect of canyon aspect ratio on canyon wind speed is included. The effect of reference wind direction relative to canyon orientation on canyon wind speed is

not yet included, however, despite its importance being emphasized in many studies (Yamartino and Wiegand 1986; Dabberdt and Hoydysh 1991; Santamouris et al. 1999; Dobre et al. 2005; Soulhac et al. 2008). These studies indicate that a reference wind that is more parallel to canyon orientation induces stronger canyon wind. In our proposed UCM, the ratio of canyon wind speed to reference wind speed is expressed in terms of canyon aspect ratio for different relative reference wind directions. To obtain equations for the ratio, a computational fluid dynamics (CFD) model is used.

In section 2, a new single-layer urban canopy model that was developed is presented. In section 3, the UCM is validated using datasets obtained at two field sites. In section 4, results of sensitivity experiments are presented. A summary is given in section 5.

2. Model description

a. Canyon wind speed

To obtain canyon wind speeds as a function of canyon aspect ratio for different reference wind directions, extensive numerical experiments are conducted using the CFD model developed by Kim and Baik (2004). The experimental setup for CFD-model simulations is described in the appendix.

Canyon-averaged wind speeds from CFD-model simulations are normalized by the reference wind speed, and a regression analysis is performed to express the canyon-averaged wind speed as a function of canyon aspect ratio for a given reference wind direction. The following fitting function in power law is considered:

$$\frac{U_c}{U_{\text{ref}}} = a \left(\frac{H}{W} \right)^b + c, \quad (1)$$

where U_c and U_{ref} are the canyon-averaged wind speed (hereinafter called canyon wind speed) and reference wind speed, respectively; a , b , and c are constants to be determined; and H/W is the canyon aspect ratio. The regression equations are as follows (Fig. 2):

$$\frac{U_c}{U_{\text{ref}}} = \begin{cases} 0.022 \left(\frac{H}{W} \right)^{-1.129} + 0.409 & \text{for } \gamma = 11.25^\circ \\ 0.058 \left(\frac{H}{W} \right)^{-0.543} + 0.311 & \text{for } \gamma = 33.75^\circ \\ 0.289 \left(\frac{H}{W} \right)^{-0.154} + 0.000 & \text{for } \gamma = 56.25^\circ \\ 0.209 \left(\frac{H}{W} \right)^{-0.302} + 0.000 & \text{for } \gamma = 78.75^\circ \end{cases}, \quad (2)$$

where γ is the reference wind direction relative to canyon orientation (Fig. A1, described in the appendix). The constants c in Eq. (1) for wind directions of 56.25° and 78.75° are not exactly zero but are sufficiently small (less than 10^{-5}). The above regression equations are valid for canyon aspect ratios between 0.25 and 5. Note that the CFD simulations are conducted under the condition of neutral thermal stratification.

Figure 2 and Eq. (2) show that for a given reference wind direction the canyon wind speed decreases as the canyon aspect ratio increases. This is consistent with results in previous studies (Swaid 1993; Lemonsu et al. 2004). For a given canyon aspect ratio, the strongest canyon wind speed appears for the most parallel wind direction ($=11.25^\circ$). For a canyon aspect ratio of 1, the regressed canyon wind speed is 43.1% (20.9%) of the reference wind speed when the relative reference wind direction is 11.25° (78.75°). The canyon wind speed for the nearly parallel wind direction is almost 2 times that for the nearly perpendicular wind direction. In the UCM, for a given reference wind direction relative to canyon orientation, two regression equations for two reference wind directions that are adjacent to the given reference wind direction in Eq. (2) are selected. Using the two regression equations, two canyon wind speeds corresponding to the

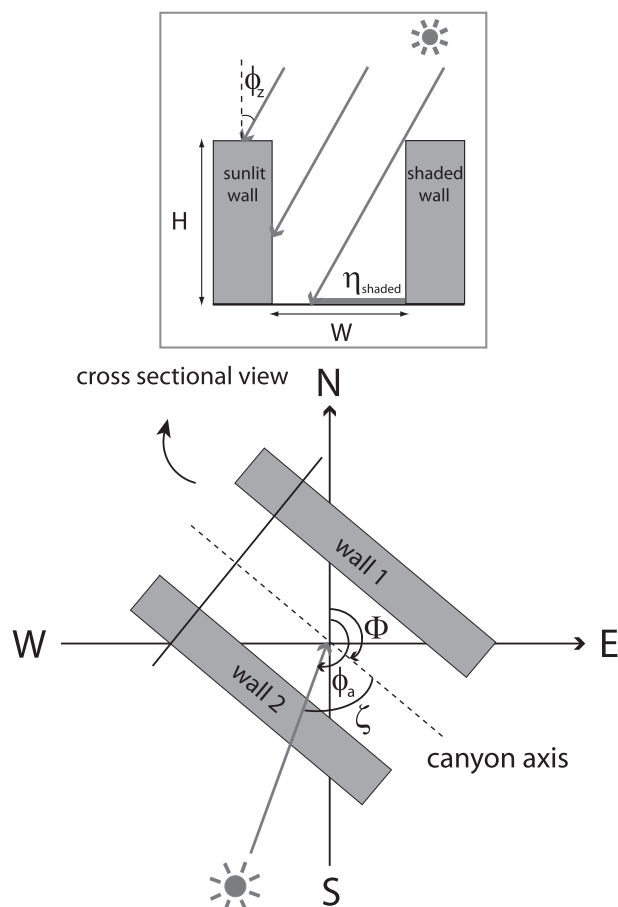


FIG. 3. A schematic diagram of the partitioning of direct shortwave radiation. Canyon orientation angle Φ and solar azimuth angle ϕ_a are measured from due north (denoted by N). Here, ϕ_z is the solar zenith angle, H is the height of walls, W is the width between the walls, and η_{shaded} is the length of the shaded road.

two reference wind directions are calculated for given canyon aspect ratio and reference wind speed. Then, a canyon wind speed for the given reference wind direction is determined through a linear interpolation/extrapolation of the two calculated canyon wind speeds.

b. Shortwave radiation

The most distinctive characteristics in the shortwave radiative transfer process in urban areas are shadow effect and multiple reflection that result from the three-dimensional structure of an urban canopy. One of the important features of our UCM is that two facing walls are dealt with separately and divided into sunlit and shaded walls. Sunlit and shaded walls are determined by solar azimuth angle and canyon orientation. When the solar azimuth angle relative to the canyon orientation [ζ in Eq. (3)] is 0° – 180° or less than -180° , wall 1 is the sunlit wall (Fig. 3):

$$\zeta = \phi_a - \Phi, \quad (3)$$

where ϕ_a is the solar azimuth angle and Φ is the canyon orientation angle. The solar zenith angle ϕ_z and azimuth angle are calculated using

$$\cos\phi_z = \sin\phi_{\text{lat}} \sin\delta + \cos\phi_{\text{lat}} \cos\delta \cos\omega_t \quad \text{and} \quad (4)$$

$$\cos\phi_a = \frac{\cos\phi_{\text{lat}} \sin\delta - \sin\phi_{\text{lat}} \cos\delta \cos\omega_t}{\sin\phi_z}, \quad (5)$$

where ϕ_{lat} is the latitude, δ is the solar declination angle, and ω_t is the hour angle. Note that the numbering of two walls illustrated in Fig. 3 does not change with canyon orientation. For example, wall 1 is the east-facing wall for a canyon orientation of 0° ($\Phi = 0^\circ$ for a north–south-oriented canyon) and is the south-facing wall for a canyon orientation of 90° ($\Phi = 90^\circ$ for an east–west-oriented canyon).

After determining sunlit and shaded walls, direct shortwave radiation incident on each surface is calculated. Incoming direct shortwave radiation on a horizontal surface at the reference height ($S^{\downarrow\text{direct}}$) is partitioned according to the length of the shaded road (η_{shaded}) (Fig. 3):

$$\eta_{\text{shaded}} = \begin{cases} H \tan\phi_z |\sin\zeta| & \text{for } \frac{H}{W} \tan\phi_z |\sin\zeta| < 1 \\ W & \text{for } \frac{H}{W} \tan\phi_z |\sin\zeta| \geq 1 \end{cases}. \quad (6)$$

If η_{shaded} is shorter than the canyon width W , both the road and one of the two walls are illuminated by sunlight. On the other hand, if η_{shaded} is equal to W , the road is completely shaded. Direct shortwave radiation incident on each surface is consequently determined as follows:

$$S_g^{\text{direct}} = \begin{cases} S^{\downarrow\text{direct}} \left(1 - \frac{H}{W} \tan\phi_z |\sin\zeta|\right) & \text{for } \frac{H}{W} \tan\phi_z |\sin\zeta| < 1 \\ 0 & \text{for } \frac{H}{W} \tan\phi_z |\sin\zeta| \geq 1 \end{cases}, \quad (7)$$

$$S_{\text{sunlit}_w}^{\text{direct}} = \begin{cases} S^{\downarrow\text{direct}} \tan\phi_z |\sin\zeta| & \text{for } \frac{H}{W} \tan\phi_z |\sin\zeta| < 1 \\ S^{\downarrow\text{direct}} \frac{W}{H} & \text{for } \frac{H}{W} \tan\phi_z |\sin\zeta| \geq 1 \end{cases}, \quad (8)$$

$$S_{\text{shaded}_w}^{\text{direct}} = 0, \quad \text{and} \quad (9)$$

$$S_r^{\text{direct}} = S^{\downarrow\text{direct}}. \quad (10)$$

Here, the subscripts g , sunlit_w , shaded_w , and r indicate the road (ground), sunlit wall, shaded wall, and roof, respectively.

The total shortwave radiation incident on each surface is a sum of the direct shortwave radiation [Eqs. (7)–(10)] and diffuse shortwave radiation. Diffuse shortwave radiation is assumed to be isotropic. Hence, the total shortwave radiation incident on each surface is given by

$$S_g = S_g^{\text{direct}} + \psi_g S^{\downarrow\text{diffuse}}, \quad (11)$$

$$S_{w1} = S_{w1}^{\text{direct}} + \psi_w S^{\downarrow\text{diffuse}}, \quad (12)$$

$$S_{w2} = S_{w2}^{\text{direct}} + \psi_w S^{\downarrow\text{diffuse}}, \quad \text{and} \quad (13)$$

$$S_r = S_r^{\text{direct}} + S^{\downarrow\text{diffuse}}. \quad (14)$$

Here, the subscripts $w1$ and $w2$ refer to wall 1 and wall 2, respectively; $S^{\downarrow\text{diffuse}}$ is the incoming diffuse shortwave radiation on a horizontal surface at the reference height; and ψ_g and ψ_w are sky-view factors at the road and wall, respectively. Following Sparrow and Cess (1978), Harman et al. (2004), Masson (2000), Lee and Park (2008), and Oleson et al. (2008), the sky-view factors are calculated using

$$\psi_g = \left[\left(\frac{H}{W} \right)^2 + 1 \right]^{1/2} - \frac{H}{W} \quad \text{and} \quad (15)$$

$$\psi_w = \frac{1}{2} \left\{ \frac{H}{W} + 1 - \left[\left(\frac{H}{W} \right)^2 + 1 \right]^{1/2} \right\} / \left(\frac{H}{W} \right). \quad (16)$$

Multiple reflection of shortwave radiation occurs among the three surfaces of the two walls and road within the canyon. Three-time reflection of shortwave radiation is adopted following Lee and Park (2008). The reflected shortwave radiation is also assumed to be isotropic; that is, the surfaces are assumed to be Lambertian. The net shortwave radiation at each surface is expressed by

$$\begin{aligned}
S_g^{\text{net}} = & S_g(1 - \alpha_g) + S_{w1}\alpha_{w1}\frac{1}{2}(1 - \psi_g)(1 - \alpha_g) + S_{w2}\alpha_{w2}\frac{1}{2}(1 - \psi_g)(1 - \alpha_g) \\
& + S_g\alpha_g\psi_w\alpha_{w1}\frac{1}{2}(1 - \psi_g)(1 - \alpha_g) + S_g\alpha_g\psi_w\alpha_{w2}\frac{1}{2}(1 - \psi_g)(1 - \alpha_g) \\
& + S_{w1}\alpha_{w1}(1 - 2\psi_w)\alpha_{w2}\frac{1}{2}(1 - \psi_g)(1 - \alpha_g) + S_{w2}\alpha_{w2}(1 - 2\psi_w)\alpha_{w1}\frac{1}{2}(1 - \psi_g)(1 - \alpha_g) \\
& + S_g\alpha_g\psi_w\alpha_{w1}(1 - 2\psi_w)\alpha_{w2}\frac{1}{2}(1 - \psi_g) + S_g\alpha_g\psi_w\alpha_{w2}(1 - 2\psi_w)\alpha_{w1}\frac{1}{2}(1 - \psi_g) \\
& + S_{w1}\alpha_{w1}\frac{1}{2}(1 - \psi_g)\alpha_g\psi_w\alpha_{w1}\frac{1}{2}(1 - \psi_g) + S_{w1}\alpha_{w1}\frac{1}{2}(1 - \psi_g)\alpha_g\psi_w\alpha_{w2}\frac{1}{2}(1 - \psi_g) \\
& + S_{w1}\alpha_{w1}(1 - 2\psi_w)\alpha_{w2}(1 - 2\psi_w)\alpha_{w1}\frac{1}{2}(1 - \psi_g) + S_{w2}\alpha_{w2}\frac{1}{2}(1 - \psi_g)\alpha_g\psi_w\alpha_{w1}\frac{1}{2}(1 - \psi_g) \\
& + S_{w2}\alpha_{w2}\frac{1}{2}(1 - \psi_g)\alpha_g\psi_w\alpha_{w2}\frac{1}{2}(1 - \psi_g) \\
& + S_{w2}\alpha_{w2}(1 - 2\psi_w)\alpha_{w1}(1 - 2\psi_w)\alpha_{w2}\frac{1}{2}(1 - \psi_g), \tag{17}
\end{aligned}$$

$$\begin{aligned}
S_{w1}^{\text{net}} = & S_{w1}(1 - \alpha_{w1}) + S_g\alpha_g\psi_w(1 - \alpha_{w1}) + S_{w2}\alpha_{w2}(1 - 2\psi_w)(1 - \alpha_{w1}) \\
& + S_g\alpha_g\psi_w\alpha_{w2}(1 - 2\psi_w)(1 - \alpha_{w1}) + S_{w1}\alpha_{w1}\frac{1}{2}(1 - \psi_g)\alpha_g\psi_w(1 - \alpha_{w1}) \\
& + S_{w1}\alpha_{w1}(1 - 2\psi_w)\alpha_{w2}(1 - 2\psi_w)(1 - \alpha_{w1}) + S_{w2}\alpha_{w2}\frac{1}{2}(1 - \psi_g)\alpha_g\psi_w(1 - \alpha_{w1}) \\
& + S_g\alpha_g\psi_w\alpha_{w1}\frac{1}{2}(1 - \psi_g)\alpha_g\psi_w + S_g\alpha_g\psi_w\alpha_{w1}(1 - 2\psi_w)\alpha_{w2}(1 - 2\psi_w) \\
& + S_g\alpha_g\psi_w\alpha_{w2}\frac{1}{2}(1 - \psi_g)\alpha_g\psi_w + S_{w1}\alpha_{w1}\frac{1}{2}(1 - \psi_g)\alpha_g\psi_w\alpha_{w2}(1 - 2\psi_w) \\
& + S_{w1}\alpha_{w1}(1 - 2\psi_w)\alpha_{w2}\frac{1}{2}(1 - \psi_g)\alpha_g\psi_w + S_{w2}\alpha_{w2}\frac{1}{2}(1 - \psi_g)\alpha_g\psi_w\alpha_{w2}(1 - 2\psi_w) \\
& + S_{w2}\alpha_{w2}(1 - 2\psi_w)\alpha_{w1}\frac{1}{2}(1 - \psi_g)\alpha_g\psi_w \\
& + S_{w2}\alpha_{w2}(1 - 2\psi_w)\alpha_{w1}(1 - 2\psi_w)\alpha_{w2}(1 - 2\psi_w), \tag{18}
\end{aligned}$$

$$\begin{aligned}
S_{w2}^{\text{net}} = & S_{w2}(1 - \alpha_{w2}) + S_g\alpha_g\psi_w(1 - \alpha_{w2}) + S_{w1}\alpha_{w1}(1 - 2\psi_w)(1 - \alpha_{w2}) \\
& + S_g\alpha_g\psi_w\alpha_{w1}(1 - 2\psi_w)(1 - \alpha_{w2}) + S_{w1}\alpha_{w1}\frac{1}{2}(1 - \psi_g)\alpha_g\psi_w(1 - \alpha_{w2}) \\
& + S_{w2}\alpha_{w2}\frac{1}{2}(1 - \psi_g)\alpha_g\psi_w(1 - \alpha_{w2}) + S_{w2}\alpha_{w2}(1 - 2\psi_w)\alpha_{w1}(1 - 2\psi_w)(1 - \alpha_{w2}) \\
& + S_g\alpha_g\psi_w\alpha_{w1}\frac{1}{2}(1 - \psi_g)\alpha_g\psi_w + S_g\alpha_g\psi_w\alpha_{w2}\frac{1}{2}(1 - \psi_g)\alpha_g\psi_w \\
& + S_g\alpha_g\psi_w\alpha_{w2}(1 - 2\psi_w)\alpha_{w1}(1 - 2\psi_w) + S_{w1}\alpha_{w1}\frac{1}{2}(1 - \psi_g)\alpha_g\psi_w\alpha_{w1}(1 - 2\psi_w) \\
& + S_{w1}\alpha_{w1}(1 - 2\psi_w)\alpha_{w2}\frac{1}{2}(1 - \psi_g)\alpha_g\psi_w + S_{w1}\alpha_{w1}(1 - 2\psi_w)\alpha_{w2}(1 - 2\psi_w)\alpha_{w1}(1 - 2\psi_w) \\
& + S_{w2}\alpha_{w2}\frac{1}{2}(1 - \psi_g)\alpha_g\psi_w\alpha_{w1}(1 - 2\psi_w) \\
& + S_{w2}\alpha_{w2}(1 - 2\psi_w)\alpha_{w1}\frac{1}{2}(1 - \psi_g)\alpha_g\psi_w, \quad \text{and} \tag{19}
\end{aligned}$$

$$S_r^{\text{net}} = S_r(1 - \alpha_r). \tag{20}$$

Here, α stands for albedo, and all of the subscripts stand for the surfaces as indicated in Eqs. (7)–(14). The last (third) reflected shortwave radiation is assumed to be totally absorbed by each surface for radiative energy

conservation. Note that the wall-view factor at the road is $(1 - \psi_g)/2$ and that the road-view factor and sky-view factor at the walls are the same, and so the wall-view factor at the other wall is $1 - 2\psi_w$. On the basis of the net

shortwave radiation at each surface, the built-up average net shortwave radiation is given by

$$S_{\text{built-up}}^{\text{net}} = f_{\text{roof}} S_r^{\text{net}} + (1 - f_{\text{roof}}) \left[S_g^{\text{net}} + \frac{H}{W} (S_{w1}^{\text{net}} + S_{w2}^{\text{net}}) \right], \quad (21)$$

where f_{roof} is the roof fraction of the built-up area.

c. Longwave radiation

One-time reflection of longwave radiation is adopted since emissivities of urban surface materials are typically high (Lee and Park 2008). All longwave radiation—that is, incoming radiation on a horizontal surface at the reference height (L^\downarrow), emitted radiation from the surfaces, and reflected radiation from the surfaces—is assumed to be isotropic. The net longwave radiation at each surface is calculated as follows:

$$\begin{aligned} L_g^{\text{net}} = & L^\downarrow \psi_g \varepsilon_g + L_{w1} \frac{1}{2} (1 - \psi_g) \varepsilon_g + L_{w2} \frac{1}{2} (1 - \psi_g) \varepsilon_g \\ & + L^\downarrow \psi_w (1 - \varepsilon_{w1}) \frac{1}{2} (1 - \psi_g) + L^\downarrow \psi_w (1 - \varepsilon_{w2}) \frac{1}{2} (1 - \psi_g) \\ & + L_g \psi_w (1 - \varepsilon_{w1}) \frac{1}{2} (1 - \psi_g) + L_g \psi_w (1 - \varepsilon_{w2}) \frac{1}{2} (1 - \psi_g) \\ & + L_{w1} (1 - 2\psi_w) (1 - \varepsilon_{w2}) \frac{1}{2} (1 - \psi_g) + L_{w2} (1 - 2\psi_w) (1 - \varepsilon_{w1}) \frac{1}{2} (1 - \psi_g) - L_g, \end{aligned} \quad (22)$$

$$\begin{aligned} L_{w1}^{\text{net}} = & L^\downarrow \psi_w \varepsilon_{w1} + L_g \psi_w \varepsilon_{w1} + L_{w2} (1 - 2\psi_w) \varepsilon_{w1} \\ & + L^\downarrow \psi_g (1 - \varepsilon_g) \psi_w + L^\downarrow \psi_w (1 - \varepsilon_{w2}) (1 - 2\psi_w) \\ & + L_g \psi_w (1 - \varepsilon_{w2}) (1 - 2\psi_w) + L_{w1} \frac{1}{2} (1 - \psi_g) (1 - \varepsilon_g) \psi_w \\ & + L_{w1} (1 - 2\psi_w) (1 - \varepsilon_{w2}) (1 - 2\psi_w) + L_{w2} \frac{1}{2} (1 - \psi_g) (1 - \varepsilon_g) \psi_w - L_{w1}, \end{aligned} \quad (23)$$

$$\begin{aligned} L_{w2}^{\text{net}} = & L^\downarrow \psi_w \varepsilon_{w2} + L_g \psi_w \varepsilon_{w2} + L_{w1} (1 - 2\psi_w) \varepsilon_{w2} \\ & + L^\downarrow \psi_g (1 - \varepsilon_g) \psi_w + L^\downarrow \psi_w (1 - \varepsilon_{w1}) (1 - 2\psi_w) \\ & + L_g \psi_w (1 - \varepsilon_{w1}) (1 - 2\psi_w) + L_{w1} \frac{1}{2} (1 - \psi_g) (1 - \varepsilon_g) \psi_w \\ & + L_{w2} \frac{1}{2} (1 - \psi_g) (1 - \varepsilon_g) \psi_w + L_{w2} (1 - 2\psi_w) (1 - \varepsilon_{w1}) (1 - 2\psi_w) - L_{w2}, \quad \text{and} \end{aligned} \quad (24)$$

$$L_r^{\text{net}} = L^\downarrow \varepsilon_r - L_r. \quad (25)$$

Here, L_i is the emitted longwave radiation from surface i ($i = g, w1, w2$, or r) according to the Stefan–Boltzmann law; that is, $L_i = \varepsilon_i \sigma T_i^4$, where ε is the surface emissivity, T is the surface temperature, and σ is the Stefan–Boltzmann constant. The first (and last) reflected longwave radiation is assumed to be totally absorbed by each surface as in the last reflected shortwave radiation. The built-up average net longwave radiation is calculated in the same way as in the built-up average net shortwave radiation [Eq. (21)].

d. Exchanges of turbulent energy and water

Turbulent energy fluxes (sensible heat flux, latent heat flux, and momentum flux) are computed according to the Monin–Obukhov similarity theory (Kot and Song 1998; Lee and Park 2008) and the Jurges formula

(Rowley et al. 1930). Turbulent energy exchanges between the canyon air and overlying atmosphere (denoted by subscript c), between the roof and overlying atmosphere (denoted by subscript r), and between the canyon air and road (denoted by subscript g) are calculated according to the Monin–Obukhov similarity theory. For example, formulas for calculating sensible heat flux $Q_{H,g}$ and latent heat flux $Q_{L,g}$ from the road (positive upward) are given by

$$\begin{aligned} Q_{H,g} = & -\rho c_p u_* \theta_* \\ = & -\rho c_p \frac{\kappa^2 U_c F_h \left(\frac{d}{z_{0m}}, \frac{d}{z_{0\theta}}, \text{Ri}_B \right)}{\ln \frac{d}{z_{0m}} \ln \frac{d}{z_{0\theta}}} (\theta_c - \theta_g) \quad \text{and} \end{aligned} \quad (26)$$

$$Q_{L,g} = -\rho\lambda u_* q_* = -\rho\lambda \frac{\kappa^2 U_c F_q \left(\frac{d}{z_{0m}}, \frac{d}{z_{0q}}, \text{Ri}_B \right)}{\ln \frac{d}{z_{0m}} \ln \frac{d}{z_{0q}}} (q_c - q_g), \quad (27)$$

where ρ is the air density; c_p is the specific heat of air at constant pressure; u_* , θ_* , and q_* are the friction velocity, turbulent potential temperature scale, and turbulent moisture scale, respectively; λ is the latent heat of vaporization; κ is the von Kármán constant; d is the displacement height (set equal to $0.65H$); and z_{0m} , $z_{0\theta}$, and z_{0q} are the roughness lengths for momentum, heat, and moisture for the road, respectively. The roughness length for moisture is set equal to that for heat. The reference height used to calculate $Q_{H,g}$ and $Q_{L,g}$ is d with an assumption that the displacement height is a representative height for the canyon air. The Ri_B is the modified bulk Richardson number defined as

$$\text{Ri}_B = gz\Delta\theta/\bar{\theta}u^2(1 - z_{0m}/z)^2/(1 - z_{0\theta}/z),$$

treating roughness lengths for momentum and heat differently. Variables θ and q stand for the potential temperature and specific humidity, respectively; and F_h and F_q are the ratios of drag coefficient for the nonneutral condition to that for the neutral condition for heat and moisture, respectively (Lee and Park 2008). The F_h (F_q) is a function of reference height (e.g., d for the road), Ri_B , z_{0m} , and $z_{0\theta}$ (z_{0q}). Turbulent fluxes from the roof and canyon air are calculated in the same way. The momentum flux expressed as ρu_*^2 is computed using u_* for the canyon air. Sensible heat flux from the walls is calculated using the Jirges formula:

$$Q_{H,w1} = (11.8 + 4.2U_c)(T_{w1} - T_c) \quad \text{and} \quad (28a)$$

$$Q_{H,w2} = (11.8 + 4.2U_c)(T_{w2} - T_c), \quad (28b)$$

where T_c is the canyon air temperature, T_{w1} is the wall-1 temperature, and T_{w2} is the wall-2 temperature. Latent heat flux from the walls is ignored since the walls are assumed to have no capability to retain water. The built-up average sensible and latent heat fluxes are computed as follows:

$$Q_{H,\text{built-up}} = f_{\text{roof}}Q_{H,r} + (1 - f_{\text{roof}})Q_{H,c} \quad \text{and} \quad (29)$$

$$Q_{L,\text{built-up}} = f_{\text{roof}}Q_{L,r} + (1 - f_{\text{roof}})Q_{L,c}. \quad (30)$$

The rainfall at the artificial surfaces is considered in the surface water budget. The maximum water capacity for the

roof and road surfaces is specified as 1 kg m^{-2} (equivalent to 1 mm). If the water amount on a surface exceeds the specified value, the rest of the water is drained out.

e. Surface and substrate temperatures

The surface and substrate temperatures are determined by solving the heat conduction equation for substrate layers. In our UCM, the grids for the temperature and conductive heat flux are staggered (Fig. 1). The conductive heat flux at the upper boundary of n th layer F_i^n , where i refers to roof, walls, or road, is given by

$$F_i^n = \begin{cases} 0 & \text{for } n = 1 \\ -k_i \frac{\partial T_i}{\partial z_p} & \text{for } 2 \leq n \leq N \\ -(S_i^{\text{net}} + L_i^{\text{net}} - Q_{H,i} - Q_{L,i}) & \text{for } n = N + 1 \end{cases}, \quad (31)$$

where k is the thermal conductivity, T is the temperature, z_p is the coordinate in the direction perpendicular to the surface, and N is the number of substrate layers. Here, the first layer is the innermost layer and the N th layer is the outermost layer. The substrate temperatures are computed using

$$C_i \frac{\partial T_i}{\partial t} = -\frac{\partial F_i}{\partial z_p}, \quad (32)$$

where C is the (volumetric) heat capacity. The surface temperature is assumed to be the same as the temperature of the outermost layer.

f. Canyon air temperature and specific humidity

The canyon air temperature T_c and specific humidity q_c are calculated using the following prognostic equations:

$$\rho c_p V_c \frac{dT_c}{dt} = \left(\frac{H}{W} Q_{H,w1} + \frac{H}{W} Q_{H,w2} + Q_{H,g} + Q_{F,c} - Q_{H,c} \right) A_c \quad \text{and} \quad (33)$$

$$\rho \lambda V_c \frac{dq_c}{dt} = (Q_{L,g} - Q_{L,c}) A_c, \quad (34)$$

where V_c is the canyon air volume, A_c is the canyon bottom area, and $Q_{F,c}$ is the anthropogenic heat flux released into the canyon.

g. Urban-averaged energy flux and urban surface energy balance

In a tile approach, an urban area is divided into two areas: a built-up area (denoted by built-up) and a natural area (denoted by natural). The natural area in the urban

TABLE 1. Urban surface parameters used to validate the UCM for Marseille and Basel.

Parameters	Marseille	Basel
Location	43.29°N, 5.38°E	47.57°N, 7.60°E
Area fractions		
Built-up area	0.864	0.840
Natural area	0.136	0.160
Geometric parameters		
Mean building height (m)	15.6	14.6
Canyon aspect ratio	1.63	1.00
Canyon orientations (°)	160 70	157 67
Roof fraction	0.69	0.54
$z_{0m}/z_{0\theta}$ for canyon air	10	10
Roof properties		
Albedo	0.22	0.14
Emissivity	0.90	0.90
Roughness length for momentum (m)	0.15	0.15
Thermal conductivity ($\text{W m}^{-1} \text{K}^{-1}$)	0.94	0.94
Heat capacity ($\text{MJ m}^{-3} \text{K}^{-1}$)	1.40	1.40
$z_{0m}/z_{0\theta}$	100	10
Wall properties		
Albedo	0.20	0.14
Emissivity	0.90	0.90
Thermal conductivity ($\text{W m}^{-1} \text{K}^{-1}$)	0.94	0.94
Heat capacity ($\text{MJ m}^{-3} \text{K}^{-1}$)	1.40	1.40
Road properties		
Albedo	0.08	0.08
Emissivity	0.94	0.94
Roughness length for momentum (m)	0.05	0.05
Thermal conductivity ($\text{W m}^{-1} \text{K}^{-1}$)	0.50	0.50
Heat capacity ($\text{MJ m}^{-3} \text{K}^{-1}$)	1.80	1.80
$z_{0m}/z_{0\theta}$	100	10

area is represented by the “Noah” land surface model (Ek et al. 2003), version 2.7.1. The two models (the urban canopy model and the Noah land surface model) are run independently. Model outputs (energy fluxes) are then area-weighted for urban-averaged energy fluxes:

$$E = f_{\text{built-up}} E_{\text{built-up}} + (1 - f_{\text{built-up}}) E_{\text{natural}}, \quad (35)$$

where E stands for all kinds of urban-averaged energy fluxes and $f_{\text{built-up}}$ is the built-up area fraction of the urban area; $E_{\text{built-up}}$ and E_{natural} correspond to the output energy fluxes from the present UCM and the Noah land surface model, respectively.

The urban surface energy balance can be given by

$$Q^* + Q_F = S^\downarrow - S^\uparrow + L^\downarrow - L^\uparrow + Q_F = Q_H + Q_L + \Delta Q_S, \quad (36)$$

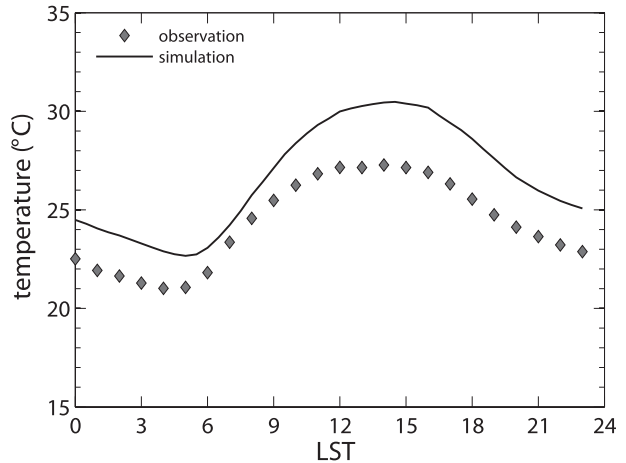


FIG. 4. Diurnal variations of observed and simulated average canyon air temperatures for Marseille. The average is taken over 24 days from 18 Jun to 11 Jul 2001, and the observed canyon air temperatures are averages over five in-canyon stations.

where Q^* , Q_F , Q_H , and Q_L are the urban-averaged net radiation, anthropogenic heat flux, sensible heat flux, and latent heat flux, respectively; S^\downarrow (S^\uparrow) and L^\downarrow (L^\uparrow) stand for the downward (upward) shortwave radiation and downward (upward) longwave radiation, respectively. The storage heat flux ΔQ_S is calculated as a residual. For the experiments in sections 3 and 4, anthropogenic heat is not included unless otherwise mentioned.

3. Validations

a. Marseille, France

Data from the urban boundary layer field campaign conducted in Marseille (Mestayer et al. 2005) are used to validate the urban canopy model. A pneumatic mast was installed on the roof of the Administrative Court of Appeal of Marseille in a dense urban area (Lemonsu et al. 2004; Grimmond et al. 2004). The temperature, humidity, wind speed and direction, pressure, upward and downward global shortwave and longwave radiation, and surface energy fluxes were measured at the site (Lemonsu et al. 2004). The observation period taken for validating the UCM is from 18 June to 11 July 2001, except for surface temperatures. Urban surface parameters used to validate the UCM for Marseille are listed in Table 1. Two canyon orientations perpendicular to each other (160° and 70°) are set as the representative canyon orientations of the city (Table 1). The following energy fluxes are averaged over the two canyon orientations. In all the experiments conducted in this study, the roof, walls, and road are composed of 10 layers [see Eq. (31)].

Figure 4 shows the diurnal variations of observed and simulated average canyon air temperatures. The observed canyon air temperature is averaged over five in-canyon

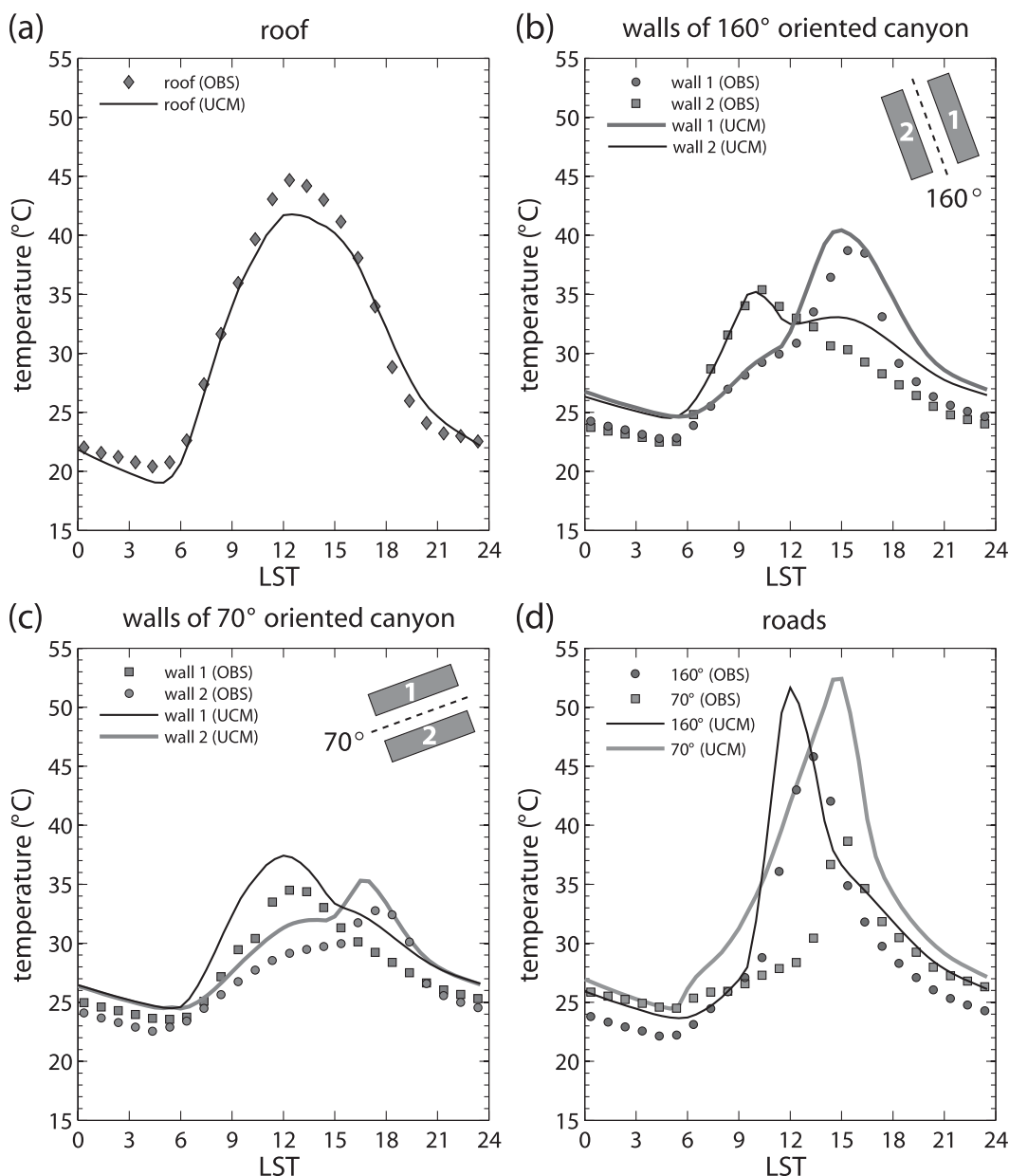


FIG. 5. Diurnal variations of observed and simulated average surface temperatures of (a) roof, (b) walls of 160°-oriented canyon, (c) walls of 70°-oriented canyon, and (d) roads for Marseille. The average is taken over 14 days from 28 Jun to 11 Jul 2001.

stations. The simulated canyon air temperature is overestimated by 2.3°C on average, and the maximum discrepancy is 3.3°C at 1600 LST. This overestimation of the canyon air temperature is also found in previous studies (Lemonsu et al. 2004; Lee and Park 2008). The geometric parameters of the canyon such as the canyon aspect ratio and canyon orientation, which would differ for the five in-canyon stations, are to some extent responsible for the overestimation of the canyon air temperature (Lemonsu et al. 2004; Lee and Park 2008).

Figure 5 shows the diurnal variations of observed and simulated average roof, wall, and road surface temperatures. The average is taken over 14 days from 28 June to 11 July 2001. The observed roof surface temperature is averaged over five tile roofs. The simulated roof surface temperature is in good agreement with the observed one except around noon (Fig. 5a). Because the two facing walls are separated in the UCM, different diurnal variations of the wall surface temperatures can be seen in Figs. 5b,c. An interesting feature is the second

peak for the simulated wall-2 surface temperature appearing at 1430 LST (Fig. 5b). This is due to the reflected shortwave and longwave radiation mainly from the opposite wall. Although the second peak of the observed wall surface temperature is not as evident as that of the simulated one, the second peak for the shaded wall surface temperature has also been simulated and observed in previous studies (Mills 1993; Idczak et al. 2007). The UCM overestimates the surface temperatures by 1.9°C for the walls and by 3.6°C for the roads [mean bias error (MBE)]. The simulated surface temperatures show good agreement in the phases, however, exhibiting increasing/decreasing patterns similar to the observed one. Some discrepancies between the simulated and observed surface temperatures can be somewhat attributed to the fact that the canyon aspect ratio and canyon orientation of each observation site are different from each other and from the model setting that is based on the area-averaged parameters near the tower.

Figure 6 shows the diurnal variations of observed and simulated average downward and upward all-wave radiation. Note that the observed downward shortwave and longwave radiative fluxes are input variables for the UCM. The UCM reproduces the upward shortwave radiation very well, whereas the upward longwave radiation is slightly overestimated. The overestimated upward longwave radiation is mainly due to the higher surface temperatures as seen in Fig. 5. This simultaneously yields an underestimation of the net radiation (see Fig. 7a).

Figure 7 shows the diurnal variations of observed and simulated average energy fluxes (net radiation, sensible heat flux, latent heat flux, and storage heat flux). Table 2 lists performance statistics for all days and under different meteorological conditions. Lemonsu et al. (2004) and Grimmond et al. (2004) classified Marseille meteorological conditions during the observation period from 18 June to 1 July 2001 into three wind regimes: “mistral,” “sea breeze,” and “other” (Dupont and Mestayer 2006). The mistral is a strong northwest katabatic wind ($>7 \text{ m s}^{-1}$), whereas the sea breeze is a light-to-moderate wind from the northwest, southwest, or southeast (Grimmond et al. 2004; Dupont and Mestayer 2006). In Table 2, all days are 169–192 (yearday); mistral days are 169, 170, 179, and 182; and sea-breeze days are 172–178 and 180–181. These partitions are made to examine performance statistics under different meteorological conditions.

On the whole, the diurnal variations of average net radiation, sensible heat flux, and storage heat flux are well simulated (Fig. 7). The simulated diurnal variation of average latent heat flux is reasonable except in the early afternoon. The UCM shows the best performances for the mistral days for all fluxes (Table 2). The root-mean-square

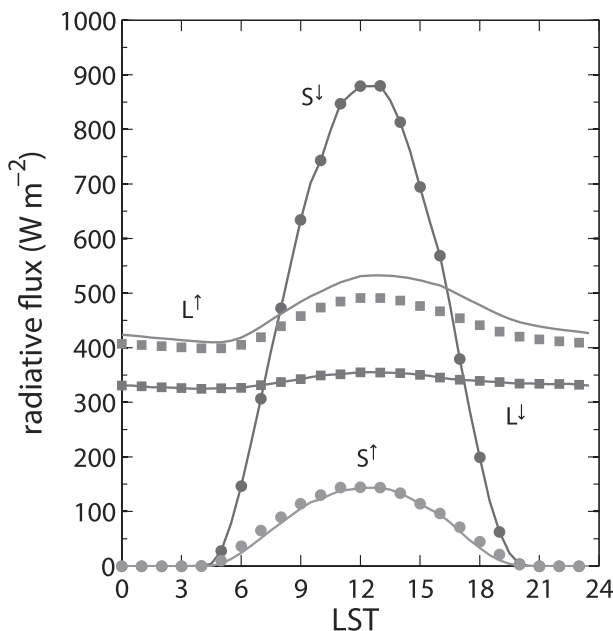


FIG. 6. Diurnal variations of observed (denoted by markers) and simulated (denoted by lines) average downward shortwave/longwave radiation ($S^{\downarrow}/L^{\downarrow}$) and upward shortwave/longwave radiation ($S^{\uparrow}/L^{\uparrow}$) for Marseille. The average is taken over 24 days from 18 Jun to 11 Jul 2001.

error (RMSE) for sensible/latent heat flux in the daytime for the mistral days is about one-half of that for the sea-breeze days. For the sea-breeze days, the observed fluxes are characterized by sudden short-term positive and negative excursions, whereas there is little excursion for the mistral days, resulting from the spatial and temporal consistency of the mistral wind and the enhanced mixing from the prevailing wind direction (Grimmond et al. 2004; Dupont and Mestayer 2006). The large RMSE for the sea-breeze days can be attributed to the large variability of the observed data, which would be influenced by large-scale advection (Dupont and Mestayer 2006). For the overall period and all days, the sensible heat flux is underestimated (Table 2), but the phase in the diurnal variation is in good agreement with the observation (Fig. 7b). Although the sensible heat flux is underestimated, it is still positive in the nighttime because the release of heat stored in urban fabrics is larger than cooling by outgoing longwave radiation, with a $\Delta Q_S/Q^*$ ratio of 1.2. For the overall period and all days, the UCM underestimates the latent heat flux by 10 W m^{-2} and overestimates the storage heat flux by 16 W m^{-2} .

To examine anthropogenic heat effects, an experiment that includes anthropogenic heat is conducted and results are compared with those of the experiment without anthropogenic heat. The anthropogenic heat flux is added with its values of $12\text{--}14 \text{ W m}^{-2}$ in the daytime

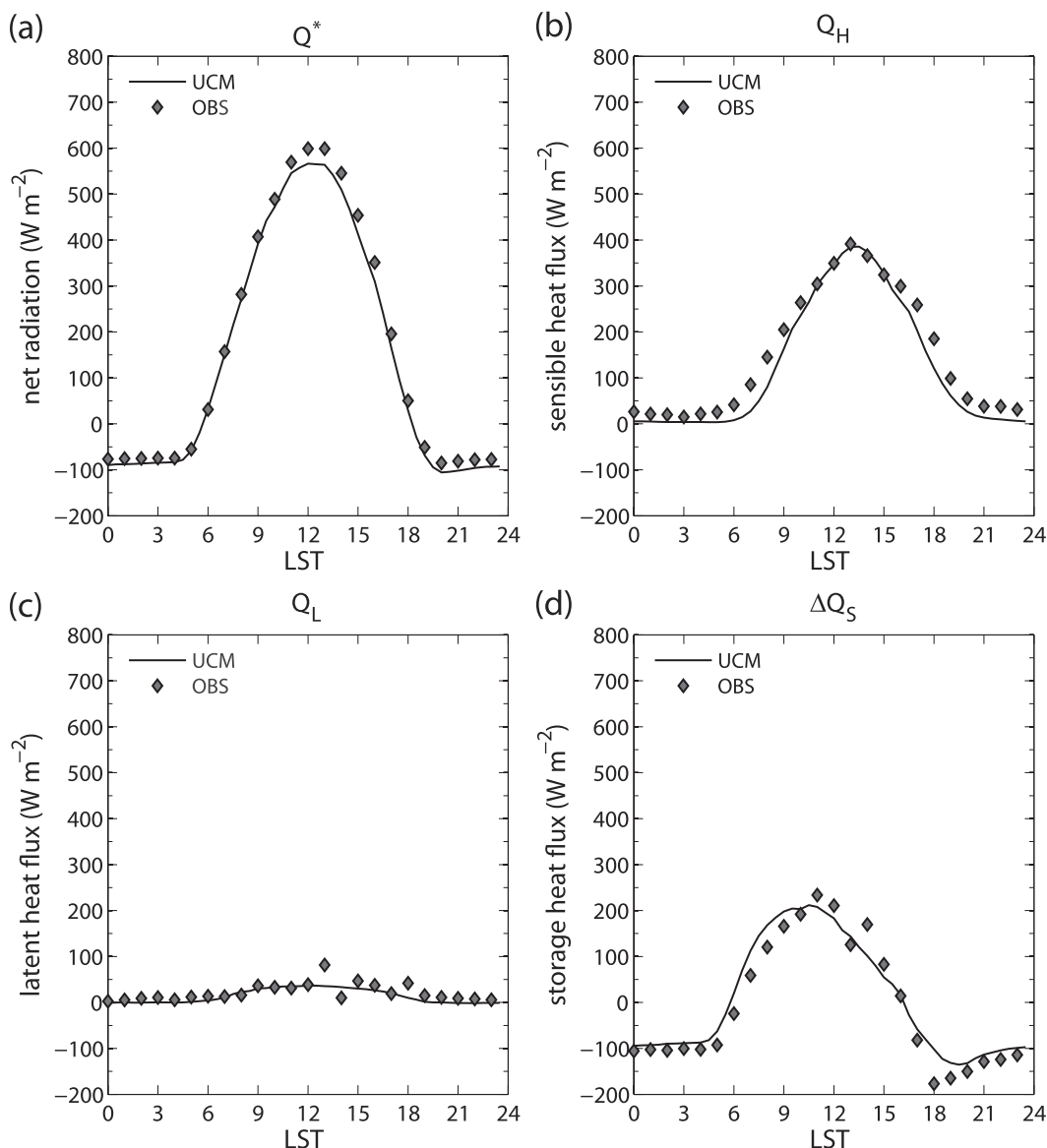


FIG. 7. Diurnal variations of observed and simulated average (a) net radiation, (b) sensible heat flux, (c) latent heat flux, and (d) storage heat flux for Marseille. The average is taken over 24 days from 18 Jun to 11 Jul 2001.

and 2 W m^{-2} in the nighttime following Lemonsu et al. (2004). For the overall period and all days, the difference in sensible heat flux between the experiments with and without anthropogenic heat is 7 W m^{-2} on average; that is, the MBE for sensible heat flux is reduced by 7 W m^{-2} when the anthropogenic heat is included. This reduction is not negligibly small. The average canyon air temperature is increased by 0.4°C .

b. Basel, Switzerland

Data from the Basel Urban Boundary Layer Experiment (BUBBLE) conducted in Basel (Rotach et al. 2005) are utilized to validate the urban canopy model.

At Ue1 (Basel-Sperrstrasse), the most urbanized site, a 30-m triangular lattice tower that was equipped with 3D-ultrasonic anemometers, temperature/humidity sensors, and full radiation instruments was set up in a street canyon (Rotach et al. 2005). To evaluate the model performance, we select 10 clear days during the intensive observation period: 13, 14, 17, 18, 19, 23, 26, and 30 June and 5 and 8 July 2002. Table 1 provides the urban surface parameters of this site.

Figure 8 shows the diurnal variations of observed and simulated average canyon air temperatures. The canyon air temperature is well reproduced in terms of phase, although its magnitude is overestimated. The simulated

TABLE 2. Performance statistics (W m^{-2}) of net radiation Q^* , sensible heat flux Q_H , latent heat flux Q_L , and storage heat flux ΔQ_S for all days, mistral days, and sea-breeze days for Marseille. See text for details. OBS and UCM refer to the mean values of observations and simulations for the period, respectively. $\text{MBE} = \text{UCM} - \text{OBS}$.

		All days				Mistral days				Sea-breeze days			
		Q^*	Q_H	Q_L	ΔQ_S	Q^*	Q_H	Q_L	ΔQ_S	Q^*	Q_H	Q_L	ΔQ_S
Overall period	OBS	160	150	23	-13	147	144	28	-25	157	139	20	-1
	UCM	140	124	13	3	137	124	19	-6	132	112	14	6
	MBE	-20	-26	-10	16	-10	-21	-9	20	-25	-26	-5	7
	RMSE	27	59	48	67	19	39	20	53	30	61	40	62
Daytime ($Q^* \geq 0$)	OBS	371	252	35	84	381	254	41	86	367	232	33	102
	UCM	345	224	24	97	370	241	36	93	332	201	28	104
	MBE	-26	-28	-11	13	-11	-13	-4	7	-34	-31	-4	2
	RMSE	34	76	62	87	22	43	24	62	38	80	50	81
Nighttime ($Q^* < 0$)	OBS	-70	39	9	-117	-77	39	16	-132	-71	37	5	-113
	UCM	-83	15	0	-98	-87	11	2	-100	-85	16	0	-101
	MBE	-14	-24	-9	19	-10	-28	-14	32	-15	-21	-6	12
	RMSE	18	32	24	36	15	34	16	44	18	30	27	29

canyon air temperature shows better performance in the nighttime than in the daytime, with MBEs of 1.9° and 3.1°C , respectively. Note that the compared canyon air temperature was observed at 2.6 m within the canyon. Because the UCM treats the canyon air as a single layer, there could be a discrepancy between the observed and simulated canyon air temperatures.

Figure 9 shows the diurnal variations of observed and simulated average downward and upward all-wave radiation. The UCM reproduces both upward shortwave and longwave radiation remarkably well except in the afternoon, with slight overestimation of the upward longwave radiation. This gives a simulated net radiation that is in very good agreement with the observed one (see Fig. 10a).

The observed and simulated average energy fluxes are shown in Fig. 10, and the corresponding performance statistics are listed in Table 3. The simulated net radiation shows the best agreement with the observed one, with an MBE of -3 W m^{-2} and an RMSE of 25 W m^{-2} for the overall period. The sensible heat flux is well reproduced in general, although it is overestimated in the afternoon. The latent heat flux is underestimated for the overall period, with the MBE being larger in its magnitude in the daytime (-25 W m^{-2}) than in the nighttime (-9 W m^{-2}). The simulated storage heat flux shows satisfactory agreement with the observed one.

Anthropogenic heat effects are examined by conducting an experiment that includes anthropogenic heat. The anthropogenic heat flux is added with its values of $12\text{--}14 \text{ W m}^{-2}$ in the daytime and 2 W m^{-2} in the nighttime as in the experiment for Marseille. For the overall period, the difference in sensible heat flux between the experiments with and without anthropogenic

heat is 7 W m^{-2} on average. That is, the MBE for sensible heat flux is increased by 7 W m^{-2} . The average canyon air temperature is increased by 0.3°C .

4. Sensitivity experiments

In this section, we examine the sensitivities of the urban surface energy balance to meteorological factors and urban surface parameters (radiative, geometric, thermal, and roughness length parameters). Only reference air temperature and wind speed are tested as meteorological factors. The reference air temperature and wind speed are assumed to vary sinusoidally and to be constant with time, respectively. The reference air temperature is set to reach a minimum at 0300 LST and a maximum at 1500 LST, with a period of 24 h. The amplitude of the

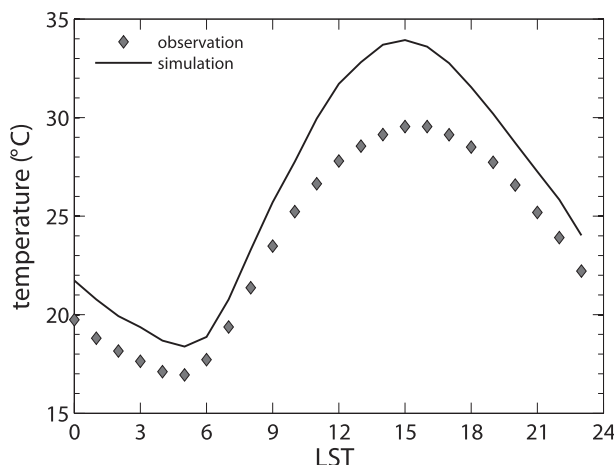


FIG. 8. Diurnal variations of observed and simulated average canyon air temperatures for Basel. The average is taken over 10 clear days: 164, 165, 168, 169, 170, 174, 177, 181, 186, and 189 (yearday).

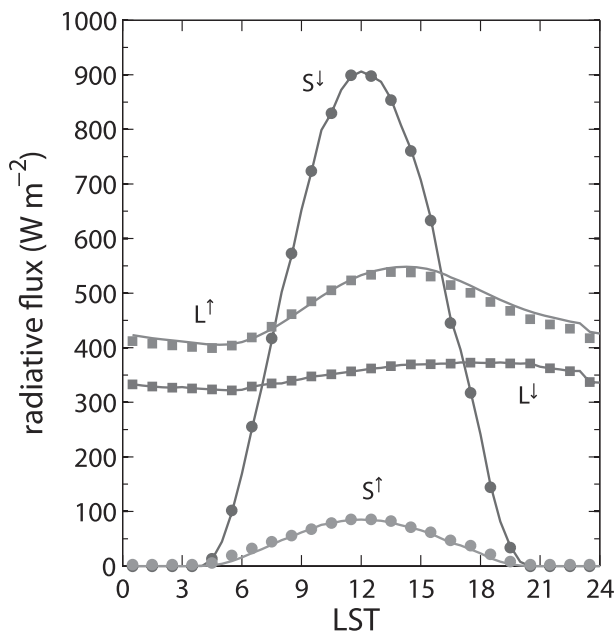


FIG. 9. Diurnal variations of observed (denoted by markers) and simulated (denoted by lines) average downward shortwave/longwave radiation ($S^\downarrow/L^\downarrow$) and upward shortwave/longwave radiation (S^\uparrow/L^\uparrow) for Basel. The average is taken over the 10 clear days.

reference air temperature is fixed to 5°C so that only the daily mean temperature \bar{T}_{ref} varies in the sensitivity experiments. The reference wind direction is specified as 45° (i.e., northeasterly wind). Five daily mean temperatures between 10° and 30°C are considered, with intervals of 5°C , and a daily mean temperature of 20°C is used for the control experiment. Six reference wind speeds between 1 and 11 m s^{-1} are tested, with intervals of 2 m s^{-1} , and a reference wind speed of 5 m s^{-1} is used for the control experiment. A formula for downward shortwave radiation proposed by Panão et al. (2007) is employed. For downward longwave radiation, a simple formula expressed as $L^\downarrow = \varepsilon_a \sigma T_{\text{ref}}^4$ is used, where ε_a is the atmospheric emissivity and T_{ref} is the air temperature at the reference height. The atmospheric emissivity is set to 0.7831. This value is based on linear regression analyses performed using the Marseille and Basel datasets.

Table 4 lists urban surface parameters in the control experiment and their ranges in the sensitivity experiments. The model is integrated for 60 h starting from 1200 LST 18 June, and data from the last 24 h are analyzed. Extensive experiments are conducted to examine the sensitivities of the urban surface energy balance to the urban surface parameters. Not all of the parameters listed in Table 4 show significant effects on energy fluxes, however (e.g., surface emissivity and $z_{0m}/z_{0\theta}$ for the road). Therefore, we present here the results for some selected

parameters with nonnegligible effects on energy fluxes: surface albedo, roof fraction, canyon aspect ratio, thermal conductivity, heat capacity, and $z_{0m}/z_{0\theta}$ for the canyon air and roof. Note that in the sensitivity experiments each parameter value varies while other parameter values remain the same as those in the control experiment.

Figure 11 shows the diurnal variations of simulated energy fluxes for various daily mean temperatures and wind speeds. The surface temperatures and accordingly the substrate temperatures increase with increasing reference air temperature. These are represented by decreases in the net longwave radiation and increases in the storage heat flux, respectively (Figs. 11c,e). According to the surface energy balance equation [Eq. (36)], increases in upward longwave radiation and storage heat flux should be balanced by a decrease in sensible heat flux, as shown in Fig. 11a. Considering the wide range of daily mean temperatures we examine, the energy fluxes are not very sensitive to the reference air temperature, however. For example, differences of $\pm 5^\circ\text{C}$ in the daily mean temperature produce ± 16 , ± 7 , and $\pm 12\text{ W m}^{-2}$ daily maximum differences in sensible heat flux, net longwave radiation, and storage heat flux, respectively, when averaged over all temperatures.

The reference wind speed directly affects the turbulent fluxes (section 2d). As the reference wind speed increases, the sensible heat flux from the surfaces or canyon air is enhanced (Fig. 11b). This enhancement is counterbalanced by decreases in both the upward longwave radiation (Fig. 11d) and storage heat flux (Fig. 11f). The degree of sensitivity of the sensible heat flux to the reference wind speed is greater than that of the net longwave radiation, by a factor of 2 at noon. Differences of $\pm 2\text{ m s}^{-1}$ in the reference wind speed produce ± 32 , ± 14 , and $\pm 19\text{ W m}^{-2}$ daily maximum differences in sensible heat flux, net longwave radiation, and storage heat flux, respectively, when averaged over all wind speeds. It is seen that weak winds ($< 5\text{ m s}^{-1}$) have a stronger impact on the energy fluxes than do strong winds. For example, at noon, a difference in sensible heat flux between reference wind speeds of 1 and 3 m s^{-1} is 51 W m^{-2} , whereas that between wind speeds of 7 and 9 m s^{-1} is 23 W m^{-2} .

Figure 12 shows daytime- and nighttime-averaged net shortwave radiation, net longwave radiation, and sensible heat flux under the variations of various urban surface parameters. As the roof albedo increases, the net shortwave radiation decreases dramatically. Because of the reduced net shortwave radiation and accordingly the decrease in the roof surface temperature, the net longwave radiation increases while the sensible heat flux decreases in both the daytime and nighttime.

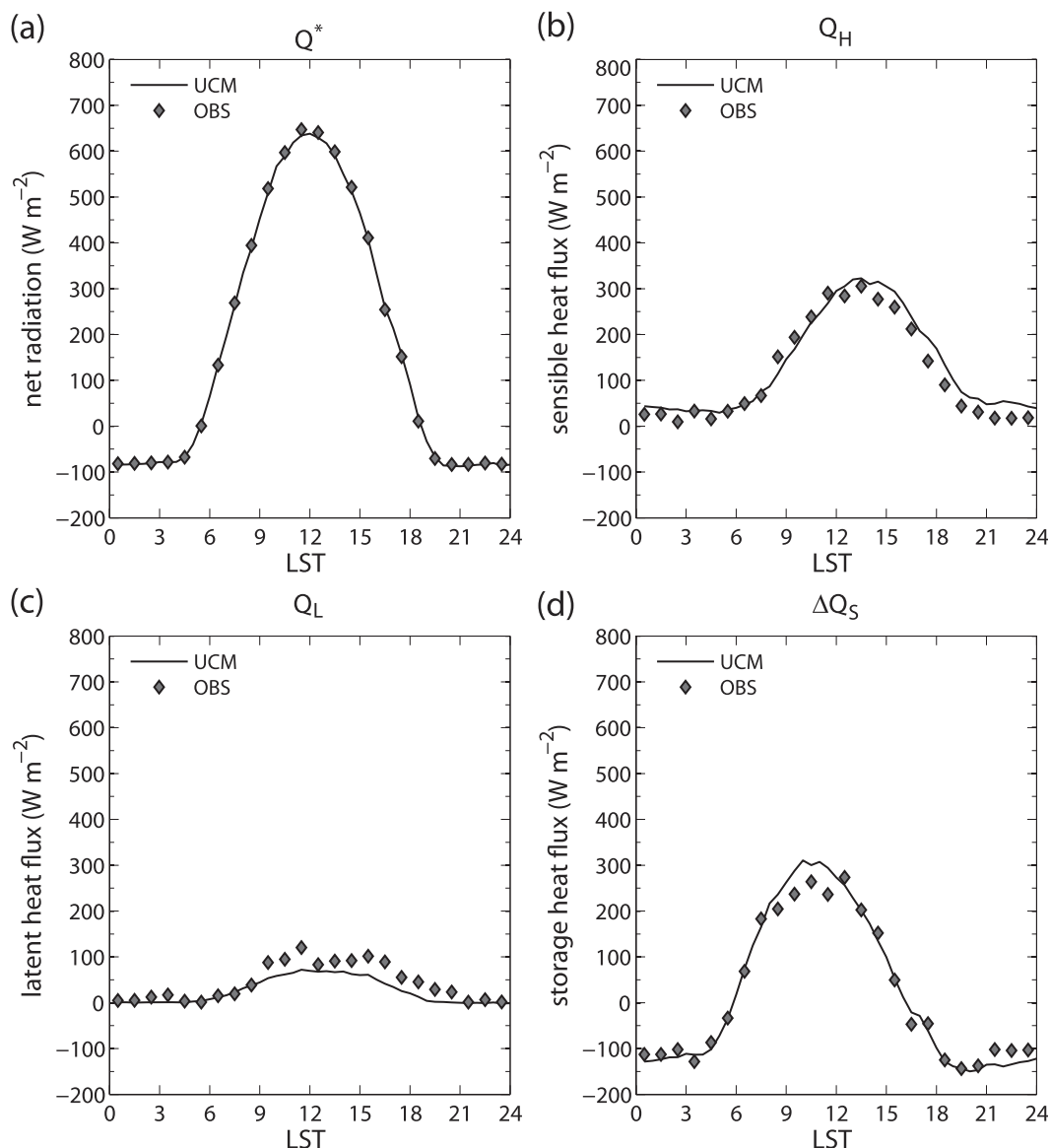


FIG. 10. Diurnal variations of observed and simulated average (a) net radiation, (b) sensible heat flux, (c) latent heat flux, and (d) storage heat flux for Basel. The average is taken over the 10 clear days.

The variations of the net longwave radiation and sensible heat flux are much more pronounced in the daytime than in the nighttime. In the wall and road albedo experiments, unlike the net shortwave radiation, the net longwave radiation and sensible heat flux show slight variations in both the daytime and nighttime. Because the energy fluxes from the roof are directly influenced by and influence the overlying atmosphere, the impact of roof albedo on the energy fluxes is much stronger than that of wall or road albedo.

The larger roof fraction yields higher urban-averaged albedo or less net shortwave radiation since the roof albedo (0.2) is larger than the effective canyon albedo (~ 0.06).

The lower effective canyon albedo is due to the shortwave radiation trapped within the canyon. The built-up average energy fluxes are calculated as the area-weighted average of the energy fluxes from the roof and canyon [Eqs. (21), (29), and (30)]. Hence, the energy fluxes from the roof are reflected more in the built-up average (and urban-averaged) energy fluxes as the roof fraction increases. Because the roof surface temperature is lower than the walls and road surface temperatures in both the daytime and nighttime, the net longwave radiation for the roof is larger than that for other surfaces within the canyon (not shown). Therefore, the urban-averaged net longwave radiation increases in both the daytime and

TABLE 3. Performance statistics (W m^{-2}) of Q^* , Q_H , Q_L , and ΔQ_S for 10 clear days for Basel.

		Q^*	Q_H	Q_L	ΔQ_S
Overall period	OBS	184	113	43	28
	UCM	181	137	26	18
	MBE	-3	25	-17	-10
	RMSE	25	51	31	55
Daytime ($Q^* \geq 0$)	OBS	400	190	72	138
	UCM	397	216	47	134
	MBE	-3	26	-25	-5
	RMSE	32	62	38	69
Nighttime ($Q^* < 0$)	OBS	-72	21	10	-102
	UCM	-73	45	1	-119
	MBE	-2	24	-9	-17
	RMSE	11	33	21	33

nighttime with increasing roof fraction. The temperature gradient between the roof and overlying atmosphere is larger (smaller) than that between the canyon air and overlying atmosphere in the daytime (nighttime) so that the sensible heat flux from the roof is larger (smaller) than that from the canyon air in the daytime (nighttime). Therefore, the sensible heat flux increases (decreases) in the daytime (nighttime) with increasing roof fraction.

In the canyon aspect-ratio experiments, the net shortwave radiation slightly increases as the canyon aspect ratio increases. This is due to the radiation-trapping effect (Masson 2000). The shortwave radiation absorbed by the walls and road per unit area decreases with increasing canyon aspect ratio, however, because of the increase in wall surface areas and the shadow effect [Eqs. (7) and (8)]. The reduced net shortwave radiation decreases the surface temperatures. This increases the daytime net longwave radiation and decreases the daytime sensible heat flux. In addition, weak wind speeds for large canyon aspect ratios [Eq. (2)] is a possible reason for the decrease in sensible heat flux in the daytime. In contrast, the nighttime net longwave radiation (sensible heat flux) decreases (increases) as the canyon aspect ratio increases. This can be explained by the increase in heat stored in the walls in the daytime since the wall surface areas increase in proportion to the canyon aspect ratio. Therefore, a large amount of heat is released in the nighttime, yielding positive and enhanced sensible heat flux for large canyon aspect ratios. Smaller sky-view factor for larger canyon aspect ratio is also responsible for the increase in surface temperature or sensible heat flux in the nighttime. This is well known as the radiation-trapping effect, especially for longwave radiation (Oke et al. 1991; Hamdi and Schayes 2008). In summary, the effect of canyon aspect ratio on the energy fluxes shows contrasting behaviors in the daytime and

TABLE 4. Urban surface parameters used in the control experiment and their ranges used in the sensitivity experiments (in square brackets).

Parameters	
Location*	45°N, 0°
Area fractions	
Built-up area	1
Natural area	0
Geometric parameters	
Mean building height (m)	20
Canyon orientations (°)	180
	90
Canyon aspect ratio	1, [0.25, 3]
Roof fraction	0.6, [0.3, 0.8]
$z_{0m}/z_{0\theta}$ for canyon air	10^2 , [10^0 , 10^4]
Roof and wall properties	
Albedo**	0.2, [0.1, 0.8]
Emissivity	0.9
Roughness length for momentum (m)	0.15
Thermal conductivity ($\text{W m}^{-1} \text{K}^{-1}$)	1.0, [0.5, 2.5]
Heat capacity ($\text{MJ m}^{-3} \text{K}^{-1}$)	1.4, [0.6, 2.6]
$z_{0m}/z_{0\theta}$ (only for roof)	10^2 , [10^0 , 10^4]
Road properties	
Albedo	0.1, [0.1, 0.8]
Emissivity	0.94
Roughness length for momentum (m)	0.05
Thermal conductivity ($\text{W m}^{-1} \text{K}^{-1}$)	0.50, [0.5, 2.5]
Heat capacity ($\text{MJ m}^{-3} \text{K}^{-1}$)	1.8, [0.6, 2.6]
$z_{0m}/z_{0\theta}$	10^2 , [10^0 , 10^4]

* The longitude of 0° is set for the convenience of calculating the LST and is not intended to indicate a specific location.

** The highest albedo (=0.8) corresponds to white-painted roof/wall or green roof (Gaffin et al. 2005). The albedos of the two walls are set to be the same.

nighttime. In the daytime, the shadow effect on the energy fluxes is more significant than the radiation-trapping effect. In the nighttime, on the other hand, a large amount of heat stored in the walls and the radiation-trapping effect lead to a decrease in net longwave radiation and an increase in sensible heat flux.

The thermal conductivity and heat capacity have similar effects on the energy fluxes in both the daytime and nighttime. As the thermal conductivity or heat capacity increases, the storage heat flux increases and the surface temperatures decrease in the daytime. As a result, the net longwave radiation (sensible heat flux) increases (decreases) as those parameters increase. In the nighttime, because of the increased storage heat flux, the surface temperatures increase (not shown). This decreases the net longwave radiation and increases the sensible heat flux in the nighttime.

The roughness lengths for momentum z_{0m} and heat $z_{0\theta}$ are important parameters for calculating sensible heat flux [Eq. (26)]. Unlike z_{0m} , which has been widely investigated in theoretical, experimental, and observational

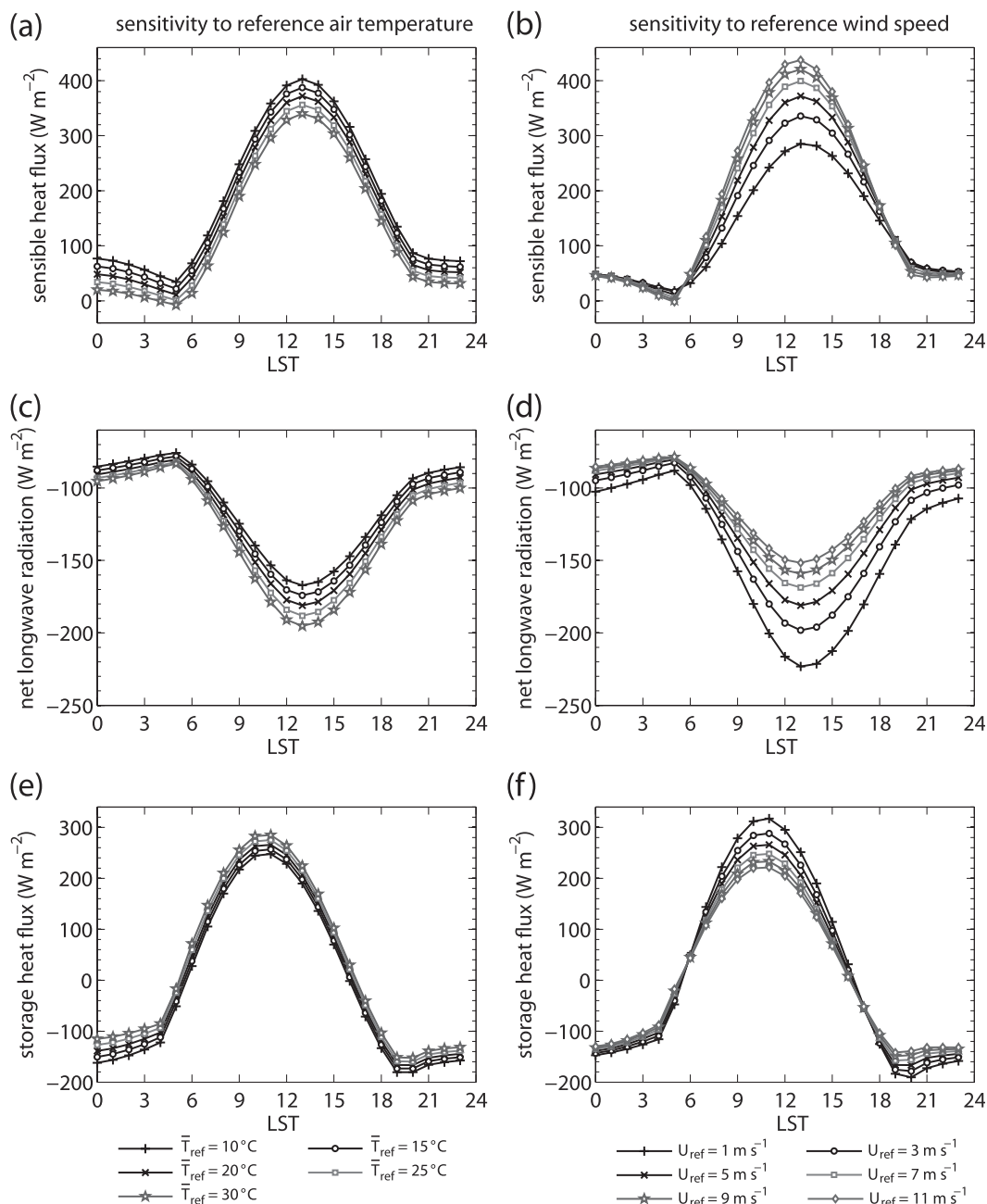


FIG. 11. Diurnal variations of (a),(b) sensible heat flux, (c),(d) net longwave radiation, and (e),(f) storage heat flux under the variations of (left) reference air temperature and (right) reference wind speed.

studies, data for $z_{0\theta}$ are relatively rare (Kanda et al. 2007). In this study, experiments are conducted with a wide range of $z_{0m}/z_{0\theta}$ values. As the ratio increases or $z_{0\theta}$ decreases, the sensible heat fluxes from the roof and canyon air decrease in the daytime (Fig. 12r). Because of the decrease in sensible heat flux, the roof surface temperature and canyon air temperature increase (not shown). This decreases the net longwave radiation in the daytime. In the nighttime, the variations of the net

longwave radiation and sensible heat flux are insignificant.

The canyon orientation is incorporated in the UCM. To examine sensitivity to canyon orientation, four experiments are conducted with different numbers of canyon orientations (1, 2, 4, and 18). The same conditions as in the control experiment are used except for a reference wind direction of 0° . The energy fluxes for one canyon orientation (90° - or 180° -oriented canyon) and

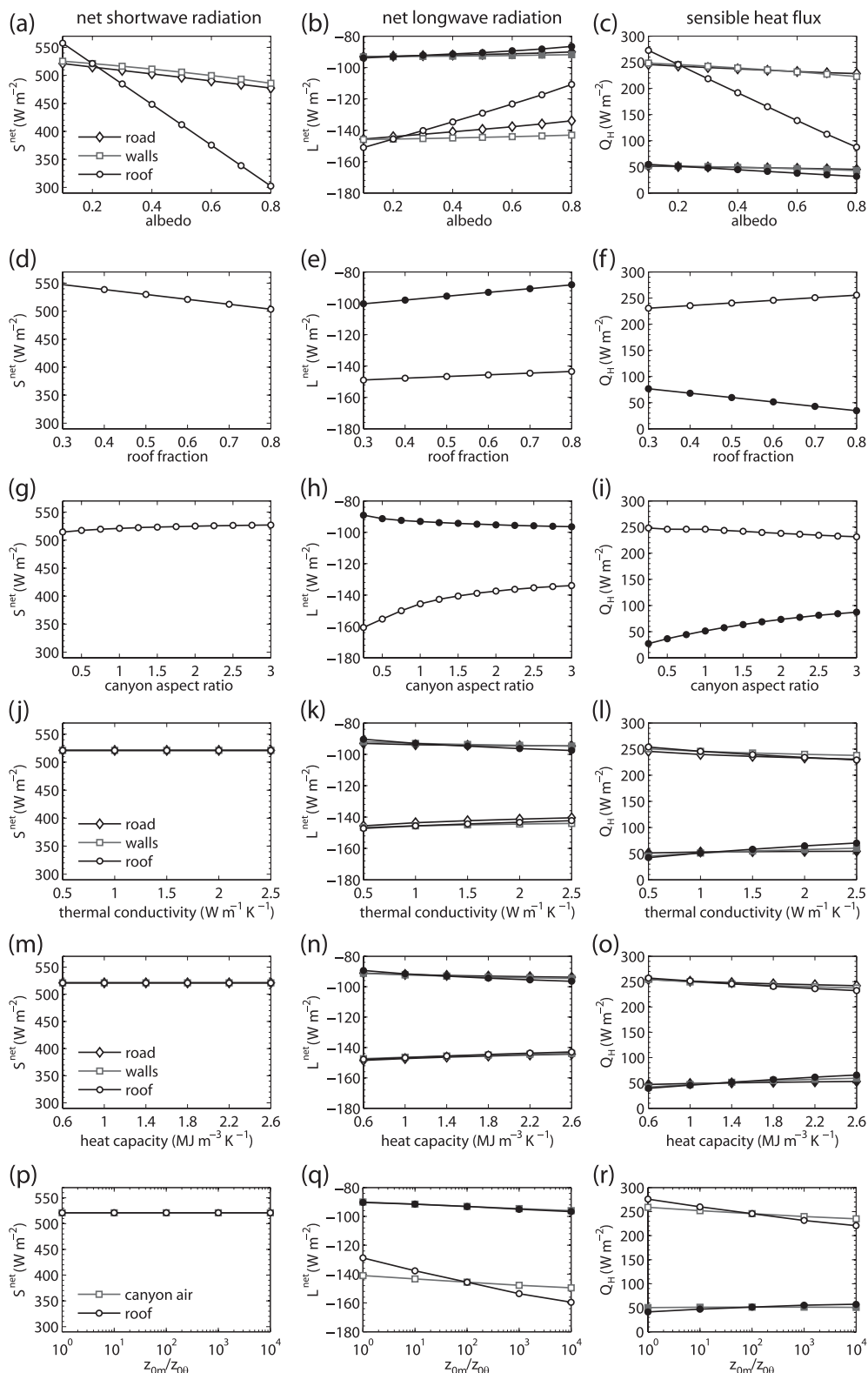


FIG. 12. Daytime-averaged (open markers) and nighttime-averaged (filled markers) (left) net shortwave radiation S_{net} , (center) net longwave radiation L_{net} , and (right) sensible heat flux Q_H under the variations of (a)–(c) albedo, (d)–(f) roof fraction, (g)–(i) canyon aspect ratio, (j)–(l) thermal conductivity, (m)–(o) heat capacity, and (p)–(r) ratio of roughness length for momentum to that for heat.

those averaged over two canyon orientations (90°- and 180°-oriented canyons), four canyon orientations (45°, 90°, 135°, and 180°-oriented canyons), and 18 canyon orientations (0°, 10°, . . . , 170°-oriented canyons with intervals of 10°) are compared. The difference in the daytime-averaged sensible heat flux between the one-canyon-orientation experiments with 90° and 180° is 11 W m^{-2} . The difference in the daytime-averaged sensible heat flux between the experiments with one canyon orientation 90° (180°) and two canyon orientations is $5.5 \text{ (5.5) W m}^{-2}$. These differences are not negligibly small. The difference in the daytime-averaged sensible heat flux between the experiments with two canyon orientations and four canyon orientations (18 canyon orientations) is $0.9 \text{ (1.0) W m}^{-2}$. These differences are small. Canyon orientation and its number for a region can be determined observationally. For example, if two perpendicular street canyons are dominant for a region, the number of canyon orientations is two. For a case of three or more dominant canyon orientations, we recommend two as the number of canyon orientations when considering computing time and sensitivity to calculated energy fluxes.

Some sensitivity experiments are conducted for Marseille and Basel. Among the urban surface parameters, roof albedo and thermal conductivity are selected. The values of the two parameters are changed by $\pm 20\%$ of their values used in the validation. The averages are taken over 24 days for Marseille and 10 clear days for Basel. For Marseille, when the roof albedo is increased (decreased) by 20%, the daytime-averaged sensible heat flux is decreased (increased) by 11 (11) W m^{-2} and the nighttime-averaged sensible heat flux is decreased (increased) by 1 (1) W m^{-2} . When the thermal conductivities of all the surfaces are increased (decreased) by 20%, the daytime-averaged sensible heat flux is decreased (increased) by 3 (4) W m^{-2} and the nighttime-averaged sensible heat flux is increased (decreased) by 2 (2) W m^{-2} . For Basel, when the roof albedo is increased (decreased) by 20%, the daytime-averaged sensible heat flux is decreased (increased) by 6 (6) W m^{-2} and the nighttime-averaged sensible heat flux is decreased (increased) by 1 (1) W m^{-2} . When the thermal conductivities of all surfaces are increased (decreased) by 20%, the daytime-averaged sensible heat flux is decreased (increased) by 5 (6) W m^{-2} and the nighttime-averaged sensible heat flux is increased (decreased) by 5 (6) W m^{-2} . For the two cities, the degrees of sensitivities to the roof albedo (also thermal conductivity) are different from each other, but increasing or decreasing trends of the sensible heat flux are similar to each other. The trends mentioned above are consistent with the results of Figs. 12c,l.

5. Summary

A more physically based single-layer urban canopy model has been developed for use in mesoscale atmospheric models. The physical processes parameterized in the UCM are the absorption and reflection of shortwave and longwave radiation, exchanges of turbulent energy and water between surfaces and adjacent air, and heat transfer by conduction through substrates. In the radiation process, two facing walls are specified as the sunlit and shaded walls according to solar azimuth angle and canyon orientation. Thus, unlike previous single-layer UCMs, surface temperatures as well as energy budgets for the four surfaces (roof, sunlit wall, shaded wall, and road) are calculated. The shadow effect and multiple reflection are included in the radiation process. The turbulent energy fluxes are calculated following the Monin–Obukhov similarity theory and the empirical formula. For better estimation of turbulent energy exchange within the canyon, equations for the ratio of canyon wind speed to reference wind speed are proposed on the basis of the simulation results from the CFD model, which reflect the effects of canyon aspect ratio and reference wind direction. The surface temperatures and canyon air temperature are explicitly calculated.

The developed model was validated by using datasets obtained at two urban sites: Marseille [Expérience sur Site pour Contraindre les Modèles de Pollution Atmosphérique et de Transport d'Emissions (ESCOMPTE) campaign], and Basel (BUBBLE campaign). The canyon air temperatures for Marseille and Basel are reasonably simulated by the UCM, with positive mean bias errors of $2^{\circ}\text{--}3^{\circ}\text{C}$. The model reproduces well the observed wall temperatures that exhibit different diurnal variations of sunlit and shaded walls depending on canyon orientation, as well as roof and road temperatures. The net radiation, sensible heat flux, latent heat flux, and storage heat flux are reproduced well by the model for both sites.

Extensive experiments were conducted to examine the sensitivities of the urban surface energy balance to meteorological factors (temperature and wind speed at a reference height) and urban surface parameters (radiative, geometric, thermal, and roughness length parameters). The impact of the reference wind speed on the energy fluxes was found to be more crucial than that of the reference air temperature, especially for weak winds. Among the urban surface parameters, the roof albedo was found to be the most sensitive parameter. The impact of canyon aspect ratio on the net longwave radiation and sensible heat flux showed contrasting behaviors in the daytime and nighttime. Of interest is that the impact of canyon aspect ratio on the energy fluxes is

similar to that of thermal conductivity and that of heat capacity both in the daytime and nighttime. The parameters related to the roof such as roof albedo, roof fraction, and ratio of roughness length for momentum to that for heat for the roof play important roles in altering urban surface energy balance since energy fluxes from the roof are directly influenced by and influence the overlying atmosphere.

Acknowledgments. The authors thank two anonymous reviewers for providing valuable comments on this work. We acknowledge that the developed model is validated using the field campaign datasets of ESCOMPTE and BUBBLE that was financed by the Swiss Ministry of Education and Science (Grant C00.0068), the University of Basel, the Swiss Federal Institute of Technology (ETH) Zürich, the Technical University of Dresden, and the Bulgarian National Institute of Meteorology and Hydrology. This work was funded by the Korea Meteorological Administration Research and Development Program under Grant CATER 2006-2202 and by the Brain Korea 21 Project (through the School of Earth and Environmental Sciences, Seoul National University).

APPENDIX

Experimental Setup of CFD-Model Simulations

A three-dimensional infinitely long street canyon is considered (Fig. A1). The width W and length L in Fig. A1 are set to 20 and 100 m, respectively. The building height H is set to 20 m for a canyon aspect ratio of 1 (control experiment) and varies according to the canyon aspect ratio H/W . The building height is calculated as a product of canyon aspect ratio and canyon width. The horizontal grid intervals are uniform with $\Delta x = 0.5$ m and $\Delta y = 1$ m. In the control experiment, the vertical grid interval is uniform with $\Delta z = 0.5$ m up to $z = 32$ m, and then it is stretched with an expansion ratio of 1.1. In the control experiment, the domain sizes are set to 50, 100, and 60.1 m in the x , y , and z directions, respectively. Note that the vertical domain size is increased to keep a constant distance between the top of the building and the top of a domain as the building height increases. The time step is set to 0.1 s, and the total integration time is 40 min. Results for the last 20 min are used for analysis.

Ten canyon aspect ratios are considered in the experiments: 0.25, 0.5, 0.75, 1, 1.5, 2, 2.5, 3, 4, and 5. Four wind directions relative to canyon orientation γ are considered: 11.25°, 33.75°, 56.25°, and 78.75°. The wind directions represent the middles of 16 cardinal directions.

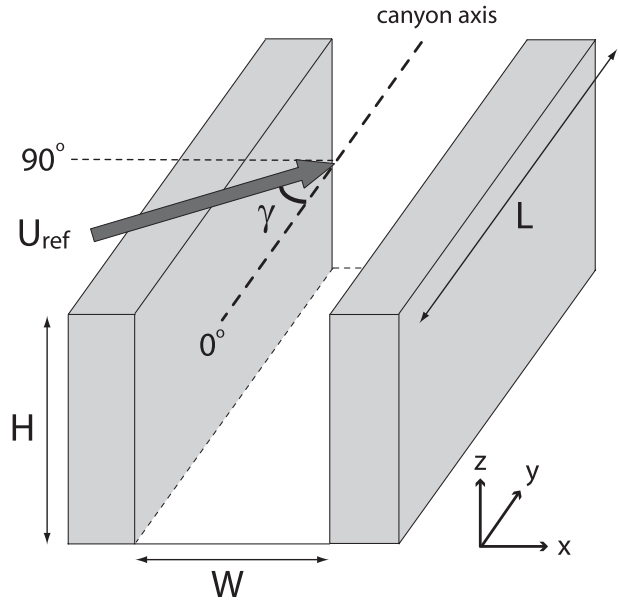


FIG. A1. Urban canyon configuration: H is the building height, W is the width between the two buildings, and L is the spanwise domain size. The thick arrow indicates the reference wind, and γ is the reference wind direction relative to canyon orientation.

The wind direction when the wind blows parallel (perpendicular) to canyon orientation is set to 0° (90°).

The inflow boundary conditions are as follows:

$$\bar{u}_0 = U_r \sin \gamma, \quad (\text{A1})$$

$$\bar{v}_0 = U_r \cos \gamma, \quad (\text{A2})$$

$$\bar{w}_0 = 0, \quad (\text{A3})$$

$$k_0 = \frac{1}{C_\mu^{1/2}} u_*^2 \left(1 - \frac{z_c}{\delta}\right)^2, \quad \text{and} \quad (\text{A4})$$

$$\varepsilon_0 = \frac{C_\mu^{3/4} k_0^{3/2}}{\kappa z_c}, \quad (\text{A5})$$

where \bar{u}_0 , \bar{v}_0 , and \bar{w}_0 are the components of the inflow reference wind velocity (its speed is denoted by U_r) in the x , y , and z directions, respectively; k_0 and ε_0 are the inflow turbulent kinetic energy and its dissipation rate, respectively; γ is the reference wind direction relative to canyon orientation; C_μ is an empirical constant ($=0.0845$); κ is the von Kármán constant ($=0.4$); u_* is the friction velocity; δ is the boundary layer depth; and z_c is a constant level ($=H + 20$ m) to set uniform inflow turbulent kinetic energy and dissipation rate. The zero-gradient condition is applied at the outflow and upper boundaries, and the periodic boundary condition is applied to the y direction. The inflow reference wind speed

is set to be uniform in the vertical direction with 5 m s^{-1} for all experiments.

Because the UCM regards the street canyon as a single layer, the canyon wind speed is averaged within the canyon. The canyon-averaged wind speed U_c is calculated using

$$U_c = \frac{1}{V_c} \int \sqrt{\bar{u}^2 + \bar{v}^2 + \bar{w}^2 + 2k} dV. \quad (\text{A6})$$

Here, V_c is the total volume of the canyon; \bar{u} , \bar{v} , and \bar{w} are the mean wind components in the x , y , and z directions, respectively; and k is the turbulent kinetic energy. Note that the CFD model used is a Reynolds-averaged Navier–Stokes equations model and that the square of the wind speed is equal to the square of the mean wind speed plus 2 times the turbulent kinetic energy. The above equation, Eq. (A6), is identical to that of Hagishima and Tanimoto (2003).

REFERENCES

- Arnfield, A. J., 2003: Two decades of urban climate research: A review of turbulence, exchanges of energy and water, and the urban heat island. *Int. J. Climatol.*, **23**, 1–26.
- Barlow, J. F., and S. E. Belcher, 2002: A wind tunnel model for quantifying fluxes in the urban boundary layer. *Bound.-Layer Meteorol.*, **104**, 131–150.
- Ca, V. T., T. Asaeda, and Y. Ashie, 1999: Development of a numerical model for the evaluation of the urban thermal environment. *J. Wind Eng. Ind. Aerodyn.*, **81**, 181–196.
- Coccal, O., and S. E. Belcher, 2004: A canopy model of mean winds through urban areas. *Quart. J. Roy. Meteor. Soc.*, **130**, 1349–1372.
- Dabberdt, W. F., and W. G. Hoydysh, 1991: Street canyon dispersion: Sensitivity to block shape and entrainment. *Atmos. Environ.*, **25A**, 1143–1153.
- Dobre, A., S. J. Arnold, R. J. Smalley, J. W. D. Boddy, J. F. Barlow, A. S. Tomlin, and S. E. Belcher, 2005: Flow field measurements in the proximity of an urban intersection in London, UK. *Atmos. Environ.*, **39**, 4647–4657.
- Dupont, S., and P. G. Mestayer, 2006: Parameterization of the urban energy budget with the submesoscale soil model. *J. Appl. Meteor. Climatol.*, **45**, 1744–1765.
- , T. L. Otte, and J. K. S. Ching, 2004: Simulation of meteorological fields within and above urban and rural canopies with a mesoscale model (MM5). *Bound.-Layer Meteorol.*, **113**, 111–158.
- Ek, M. B., K. E. Mitchell, Y. Lin, E. Rogers, P. Grunmann, V. Koren, G. Gayno, and J. D. Tarpley, 2003: Implementation of Noah land surface model advances in the National Centers for Environmental Prediction operational mesoscale Eta Model. *J. Geophys. Res.*, **108**, 8851, doi:10.1029/2002JD003296.
- Gaffin, S., C. Rosenzweig, L. Parshall, D. Beattie, R. Berghage, G. O’Keefe, and D. Braman, 2005: Energy balance modeling applied to a comparison of white and green roof cooling efficiency. *Proc. Third North American Green Roof Conf.: Greening Rooftops for Sustainable Communities*, Washington, DC, The Cardinal Group, 583–597.
- Grimmond, C. S. B., J. A. Salmond, T. R. Oke, B. Offerle, and A. Lemonsu, 2004: Flux and turbulence measurements at a densely built-up site in Marseille: Heat, mass (water and carbon dioxide), and momentum. *J. Geophys. Res.*, **109**, D24101, doi:10.1029/2004JD004936.
- Hagishima, A., and J. Tanimoto, 2003: Field measurements for estimating the convective heat transfer coefficient at building surfaces. *Build. Environ.*, **38**, 873–881.
- Hamdi, R., and G. Schayes, 2008: Sensitivity study of the urban heat island intensity to urban characteristics. *Int. J. Climatol.*, **28**, 973–982.
- Harman, I. N., M. J. Best, and S. E. Belcher, 2004: Radiative exchange in an urban street canyon. *Bound.-Layer Meteorol.*, **110**, 301–316.
- Idczak, M., P. Mestayer, J.-M. Rosant, J.-F. Sini, and M. Violleau, 2007: Micrometeorological measurements in a street canyon during the joint ATREUS–PICADA experiment. *Bound.-Layer Meteorol.*, **124**, 25–41.
- Kanda, M., 2007: Progress in urban meteorology: A review. *J. Meteor. Soc. Japan*, **85B**, 363–383.
- , M. Kanega, T. Kawai, and R. Moriawaki, 2007: Roughness lengths for momentum and heat derived from outdoor urban scale models. *J. Appl. Meteor. Climatol.*, **46**, 1067–1079.
- Kim, J.-J., and J.-J. Baik, 1999: A numerical study of thermal effects on flow and pollutant dispersion in urban street canyons. *J. Appl. Meteor.*, **38**, 1249–1261.
- , and —, 2004: A numerical study of the effects of ambient wind direction on flow and dispersion in urban street canyons using the RNG k – ϵ turbulence model. *Atmos. Environ.*, **38**, 3039–3048.
- Kondo, H., Y. Genchi, Y. Kikegawa, Y. Ohashi, H. Yoshikado, and H. Komiyama, 2005: Development of a multi-layer urban canopy model for the analysis of energy consumption in a big city: Structure of the urban canopy model and its basic performance. *Bound.-Layer Meteorol.*, **116**, 395–421.
- Kot, S. C., and Y. Song, 1998: An improvement of the Louis scheme for the surface layer in an atmospheric modelling system. *Bound.-Layer Meteorol.*, **88**, 239–254.
- Kusaka, H., H. Kondo, Y. Kikegawa, and F. Kimura, 2001: A simple single-layer urban canopy model for atmospheric models: Comparison with multi-layer and slab models. *Bound.-Layer Meteorol.*, **101**, 329–358.
- Lee, I. Y., and H. M. Park, 1994: Parameterization of the pollutant transport and dispersion in urban street canyons. *Atmos. Environ.*, **28**, 2343–2349.
- Lee, S.-H., and S.-U. Park, 2008: A vegetated urban canopy model for meteorological and environmental modelling. *Bound.-Layer Meteorol.*, **126**, 73–102.
- Lemonsu, A., C. S. B. Grimmond, and V. Masson, 2004: Modeling the surface energy balance of the core of an old Mediterranean city: Marseille. *J. Appl. Meteor.*, **43**, 312–327.
- Martilli, A., A. Clappier, and M. W. Rotach, 2002: An urban surface exchange parameterization for mesoscale models. *Bound.-Layer Meteorol.*, **104**, 261–304.
- Masson, V., 2000: A physically-based scheme for the urban energy budget in atmospheric models. *Bound.-Layer Meteorol.*, **94**, 357–397.
- , 2006: Urban surface modeling and the meso-scale impact of cities. *Theor. Appl. Climatol.*, **84**, 35–45.
- Mestayer, P. G., and Coauthors, 2005: The urban boundary-layer field campaign in Marseille (UBL/CLU-ESCOMPTE): Set-up and first results. *Bound.-Layer Meteorol.*, **114**, 315–365.

- Mills, G. M., 1993: Simulation of the energy budget of an urban canyon—I. Model structure and sensitivity test. *Atmos. Environ.*, **27B**, 157–170.
- Oke, T. R., G. T. Johnson, D. G. Steyn, and I. D. Watson, 1991: Simulation of surface urban heat islands under ‘ideal’ conditions at night. Part 2: Diagnosis of causation. *Bound.-Layer Meteor.*, **56**, 339–358.
- Oleson, K. W., G. B. Bonan, J. Feddema, M. Vertenstein, and C. S. B. Grimmond, 2008: An urban parameterization for a global climate model. Part I: Formulation and evaluation for two cities. *J. Appl. Meteor. Climatol.*, **47**, 1038–1060.
- Otte, T. L., A. Lacser, S. Dupont, and J. K. S. Ching, 2004: Implementation of an urban canopy parameterization in a mesoscale meteorological model. *J. Appl. Meteor.*, **43**, 1648–1665.
- Panão, M. J. N. O., H. J. P. Gonçalves, and P. M. C. Ferrão, 2007: A matrix approach coupled with Monte Carlo techniques for solving the net radiative balance of the urban block. *Bound.-Layer Meteor.*, **122**, 217–241.
- Rotach, M. W., and Coauthors, 2005: BUBBLE—An urban boundary layer meteorology project. *Theor. Appl. Climatol.*, **81**, 231–261.
- Roth, M., 2000: Review of atmospheric turbulence over cities. *Quart. J. Roy. Meteor. Soc.*, **126**, 941–990.
- Rowley, F. B., A. B. Algren, and J. L. Blackshaw, 1930: Surface conductances as affected by air velocity, temperature, and character of surface. *ASHRAE Trans.*, **36**, 429–446.
- Santamouris, M., N. Papanikolaou, I. Koronakis, I. Livada, and D. Asimakopoulos, 1999: Thermal and air flow characteristics in a deep pedestrian canyon under hot weather conditions. *Atmos. Environ.*, **33**, 4503–4521.
- Shepherd, J. M., 2005: A review of current investigations of urban-induced rainfall and recommendations for the future. *Earth Interact.*, **9**. [Available online at <http://EarthInteractions.org>.]
- Soulhac, L., R. J. Perkins, and P. Salizzoni, 2008: Flow in a street canyon for any external wind direction. *Bound.-Layer Meteor.*, **126**, 365–388.
- Sparrow, E. M., and R. D. Cess, 1978: *Radiation Heat Transfer*. Hemisphere, 366 pp.
- Swaid, H., 1993: The role of radiative-convective interaction in creating the microclimate of urban street canyons. *Bound.-Layer Meteor.*, **64**, 231–259.
- Yamartino, R. J., and G. Wiegand, 1986: Development and evaluation of simple models for the flow, turbulence and pollutant concentration fields within an urban street canyon. *Atmos. Environ.*, **20**, 2137–2156.